

# Adaptive Temporal Gating of Longitudinal Magnetic Resonance Imaging for Alzheimer’s Prediction

Alireza Moayedikia<sup>a,\*</sup>, Sara Fin<sup>b</sup>, Alicia Troncoso<sup>c</sup>, Uffe Kock Wiil<sup>d</sup>, for the Alzheimer’s Disease Neuroimaging Initiative<sup>1</sup>

<sup>a</sup>*School of Business Law and Entrepreneurship, Swinburne University of Technology, Melbourne, VIC, Australia*

<sup>b</sup>*Australian Regenerative Medicine Institute, Monash University, Melbourne, VIC, Australia*

<sup>c</sup>*Data Science & Big Data Lab, Universidad Pablo de Olavide, Seville, Spain*

<sup>d</sup>*The Maersk Mc-Kinney Møller Institute, University of Southern Denmark, Odense, Denmark*

---

## Abstract

Predicting the conversion from Mild Cognitive Impairment (MCI) to Alzheimer’s Disease (AD) is critical for early therapeutic intervention. While deep learning has demonstrated considerable efficacy in automated neuroimaging analysis, current paradigms predominantly rely on cross-sectional structural Magnetic Resonance Imaging (MRI), inherently neglecting the prognostic value embedded in patient-specific anatomical trajectories over time. To overcome this limitation, we introduce the Temporal Adaptive Fusion Network (TAF-Net), a novel hybrid architecture that combines convolutional and transformer-based components to comprehensively model paired longitudinal three-dimensional MRI scans. Central to TAF-Net is a dedicated Temporal Fusion Module governed by an Adaptive Temporal Gate, which dynamically learns patient-specific weightings to optimally synthesise three distinct spatiotemporal representations: explicit structural deformation, region-to-region temporal cross-attention, and comprehensive bilateral feature concatenation. We extensively evaluated the proposed framework on the Alzheimer’s Disease Neuroimaging Initiative cohort for the task of predicting three-year MCI-to-AD conversion. Under stringent subject-level cross-validation, TAF-Net achieved the highest discriminative performance among all evaluated methods using only structural MRI, significantly outperforming the strongest baseline and approaching multimodal methods that additionally require positron emission tomography, cerebrospinal fluid, or genetic data. Notably, the architecture exhibited exceptional data efficiency, matching or exceeding baseline performance with a small fraction of the training data. Through rigorous ablation, we empirically demonstrate that incorporating longitudinal information via the adaptive gating mechanism not only improves overall discrimination but also substantially reduces predictive variance compared to single-timepoint evaluations, conferring enhanced model stability. Furthermore, interpretability analyses reveal that the network’s spatial attention biologically aligns with established Alzheimer’s pathology in the medial temporal lobe and ventricles. The gating mechanism itself heavily prioritises explicit volumetric change, demonstrating a strong positive correlation with clinical conversion risk.

**Keywords:** Alzheimer’s disease, Deep learning, Longitudinal MRI, Medical image analysis, Temporal fusion, Vision-Transformers

---

\*Corresponding author: Alireza Moayedikia (PhD) is with the department of Business Technology and Entrepreneurship of Swinburne University of Technology, John Street, Hawthorn 3122, VIC, Australia – Email: amoayedikia@swinburne.edu.au

<sup>1</sup>Data used in preparation of this article were obtained from the Alzheimer’s Disease Neuroimaging Initiative (ADNI) database (adni.loni.usc.edu). As such, the investigators within the ADNI contributed to the design and implementation of ADNI and/or provided data but did not participate in analysis or writing of this report. A complete listing of ADNI investigators can be found at: [http://adni.loni.usc.edu/wp-content/uploads/how\\_to\\_apply/ADNI\\_Acknowledgement\\_List.pdf](http://adni.loni.usc.edu/wp-content/uploads/how_to_apply/ADNI_Acknowledgement_List.pdf)

## 1. Introduction

Alzheimer’s disease (AD) is a progressive brain disorder that gradually destroys memory and cognitive function, and it represents the most common cause of dementia worldwide [1]. The disease begins silently, often years or even decades before symptoms appear. During this hidden phase, two abnormal proteins accumulate in the brain: amyloid- $\beta$  plaques and tau tangles, changes that eventually lead to widespread neuronal loss [2]. Crucially, amyloid deposition precedes tau pathology, yet it is tau accumulation and the accompanying brain atrophy that correlate most closely with cognitive decline [2, 3]. The observation that a substantial proportion of cognitively normal elderly individuals already harbor significant amyloid pathology underscores the existence of a prolonged preclinical window—one that offers both diagnostic challenges and therapeutic opportunities [2].

This preclinical window reflects the recognition that AD unfolds over a prolonged timeline, progressing through distinct clinical stages. The first is the preclinical stage, where individuals are cognitively normal but show biological evidence of AD, detectable through biomarkers of amyloid deposition, neurodegeneration, or both [4]. The second stage is mild cognitive impairment (MCI), the symptomatic prodementia phase in which patients show concern about cognitive changes and have measurable impairment—typically in memory—yet can still function independently and do not meet criteria for dementia [5]. MCI is common among older adults and represents a critical window for potential intervention [6].

A major clinical challenge is that MCI outcomes vary widely. Meta-analyses reveal that while a substantial proportion of MCI patients progress to dementia, many remain stable, and some even return to normal cognition [7]. Conversion rates differ between specialist clinics and community settings, and vary further depending on patient characteristics and diagnostic methods [8]. The amnesic subtype of MCI most commonly progresses to AD, whereas non-amnesic subtypes may lead to other forms of dementia [6]. This heterogeneity challenges the assumption that MCI is simply early-stage dementia and underscores the need for accurate prediction tools to identify individuals who will benefit most from early intervention.

Structural MRI is a valuable tool for detecting and tracking brain degeneration in AD. Brain shrinkage in AD follows a predictable pattern, beginning in the medial temporal lobe—particularly the hippocampus and entorhinal cortex—then spreading to the temporal neocortex, posterior cingulate, and precuneus, and eventually affecting widespread cortical regions [9]. This pattern mirrors the spread of tau pathology and provides the basis for using MRI to stage disease severity and predict outcomes.

The hippocampus and entorhinal cortex have received particular attention as early markers of AD-related brain changes. Prospective studies show that smaller volumes in these regions independently predict conversion from MCI to AD, with the hippocampus showing stronger predictive value than the entorhinal cortex [10]. These volumes show a clear gradient across diagnostic groups: largest in cognitively normal controls, intermediate in stable MCI, and smallest in MCI patients who later convert to AD [10]. Beyond volume measures, cortical thickness analysis has identified a consistent “AD signature” that includes the medial temporal cortex, temporal pole, inferior temporal gyrus, lateral parietal cortex, and precuneus [11]. Importantly, this signature appears not only in mild AD dementia but also in cognitively normal older adults who have amyloid pathology, establishing cortical thickness as an early marker of future decline [11].

Longitudinal MRI studies show that rates of brain shrinkage provide information beyond what single scans can capture. In healthy elderly individuals, faster ventricular expansion predicts conversion to MCI or AD, and in MCI subjects, both ventricular and whole-brain shrinkage rates predict subsequent AD conversion [12]. Combining baseline hippocampal volume with longitudinal shrinkage rates provides complementary information, as both the current state of brain degeneration and its trajectory contribute to prognosis [12].

These dynamic changes have been rigorously validated by large-scale multicenter efforts, most notably the Alzheimer’s Disease Neuroimaging Initiative (ADNI). Studies leveraging this comprehensive public dataset have confirmed that ventricular enlargement serves as an objective and sensitive progression

marker, with AD subjects showing substantially greater expansion over six months compared to controls [13]. Furthermore, longitudinal tracking within these large cohorts reveals that MCI patients who later convert to AD exhibit shrinkage rates approaching those seen in established AD, especially for the hippocampus and entorhinal cortex [14]. Comprehensive reviews have established longitudinal structural MRI as the most efficient outcome measure for clinical trials, outperforming cognitive tests [15].

Multiple biomarker types have been studied for predicting MCI-to-AD progression, including cerebrospinal fluid markers, blood-based assays, and positron emission tomography [1, 16]. While some of these approaches show strong prognostic accuracy, they involve greater cost, require invasive collection procedures, or have limited availability outside academic centers. Structural MRI, by contrast, is widely accessible, non-invasive, and routinely acquired in clinical practice, making it an attractive foundation for scalable prediction tools—yet it has been studied primarily using single scans, an approach that may miss the dynamic, progressive nature of AD neurodegeneration.

While clinical and biomarker research has firmly established the value of structural MRI, the computational analysis of these images has historically relied on single-timepoint snapshots. Early machine learning approaches have achieved strong diagnostic performance in distinguishing AD from healthy controls, but predicting which MCI patients will progress to AD dementia remains substantially more challenging. This performance gap reflects both the subtlety of prodromal changes and genuine biological heterogeneity within the MCI population. For instance, studies using clinically transferable features—cognitive scores, hippocampal volumes, and APOE status—have identified a consistent “hard to classify” subgroup of MCI patients whose progression is difficult to model, suggesting genuine biological divergence [17].

A fundamental limitation of most computational studies is their reliance on baseline imaging alone. Recent studies directly addressing this gap have demonstrated that longitudinal approaches—such as combining CNN embeddings with Time-Aware LSTMs for survival analysis—substantially outperform single-timepoint models [18]. This confirms that temporal patterns of brain change carry prognostic information beyond what can be captured from a single scan. However, these foundational longitudinal studies have predominantly used older architectures that lack mechanisms for modeling long-range spatial dependencies across the brain, leaving significant room for architectural advancement.

The evidence reviewed above reveals critical gaps at the intersection of clinical neuroimaging and computational methodology. From the clinical perspective, longitudinal shrinkage rates consistently outperform single-scan measures for prognosis [12, 14], and computational validation has confirmed that temporal modeling substantially improves prediction [18]. From the methodological perspective, hybrid CNN-Transformer architectures represent the current state-of-the-art for AD classification, achieving high accuracy under rigorous evaluation [19, 20, 21].

However, these two advances have not been adequately combined. Existing longitudinal approaches have relied on older architectures lacking mechanisms for modeling long-range spatial dependencies across brain regions, while modern hybrid CNN-Transformer architectures have been applied exclusively to single-timepoint data. The present study addresses these gaps through three primary contributions.

First, we develop a hybrid CNN-Transformer architecture with temporal attention that processes paired MRI scans (baseline and 12-month follow-up) to predict 3-year MCI-to-AD conversion, combining modern spatial modeling with longitudinal data. Second, we provide a direct comparison of longitudinal versus baseline-only models using identical architectures and evaluation protocols, isolating the added prognostic value of temporal information. Third, we analyze attention patterns to identify which brain regions and temporal changes drive predictions, providing the interpretable insights necessary for clinical adoption.

The remainder of this paper is organized as follows. Section 2 provides a comprehensive review of deep learning techniques for AD classification and analyzes the critical design choices in longitudinal architectures. Section 3 describes the dataset, preprocessing pipeline, and quality control procedures applied to all MRI volumes. Section 4 details the proposed TAF-Net methodology, describing the Siamese encoder, the novel Temporal Fusion Module, and the adaptive gating mechanism. Section 5 specifies the evaluation

protocol, benchmark methods, and training strategy. Section 6 presents the experimental results, including comparative performance, ablation studies, and interpretability analyses. Section 7 discusses clinical implications, biological plausibility, limitations, and future directions, and Section 8 concludes the paper.

## 2. Literature Review

The application of deep learning to structural MRI has fundamentally transformed the landscape of Alzheimer’s disease classification and prognosis. However, the architectural requirements for diagnosing AD from a single scan differ substantially from those needed to predict future cognitive decline based on morphological changes over time. To contextualize the contributions of our proposed Temporal Attention Fusion Network (TAF-Net) architecture, this section reviews the progression of deep learning methodologies in this domain. We divide our review into two key areas: first, we examine the evolution of models applied to single-timepoint MRI, tracing the development from standard 3D Convolutional Neural Networks to modern Vision Transformers and hybrid architectures. Second, we focus specifically on longitudinal architectures, systematically analyzing the design choices—such as fusion topologies and attention mechanisms—that govern how temporal image pairs are integrated to model disease progression.

Early applications of deep learning to structural MRI for AD classification were marked by methodological concerns, particularly data leakage from 2D slice-based approaches that inflated reported accuracy [22]. Subsequent work using rigorous subject-level cross-validation and 3D volumetric processing has demonstrated genuine improvements. Efficient lightweight 3D CNNs with dilated convolutions achieved strong performance for AD versus CN classification with external validation across multiple datasets [23]. Custom 3D CNNs validated externally on the National Alzheimer’s Coordinating Center (NACC) cohort showed good discriminative ability for distinguishing cognitively normal subjects from those with MCI or mild AD [24]. Importantly, MCI subjects misclassified as AD by deep learning models showed faster real-world progression to dementia, suggesting that predictions may carry prognostic value beyond diagnostic accuracy [24]. Multi-scale attention-based pseudo-3D CNNs have been proposed to balance computational efficiency with volumetric processing, achieving competitive performance while reducing memory requirements [25]. Whole-brain 3D CNN approaches processing complete MRI volumes without prior feature selection have shown that end-to-end learning can identify discriminative patterns beyond traditional regions of interest [26].

Despite these advances, achieving clinically meaningful generalization remains an open challenge. Ensemble methods combining multiple architectures have reported high accuracy on ADNI but consistent performance drops on external clinical validation [27]. Furthermore, while CNNs excel at extracting local spatial features, they struggle to capture long-range dependencies across brain regions—a limitation particularly relevant for AD, where distributed atrophy patterns span multiple anatomical structures. Vision Transformers (ViTs), which process images as sequences of patches using self-attention mechanisms, offer a potential solution by modeling global relationships. However, pure transformer architectures require large training datasets to achieve optimal performance, presenting challenges for medical imaging.

Hybrid architectures combining CNNs with Vision Transformers have emerged to leverage the complementary strengths of both approaches. Conv-Swinformer integrates VGGNet-16 for low-level feature extraction with a Swin Transformer encoder, achieving high accuracy for AD classification and reasonable performance for the more challenging CN versus MCI distinction [19]. Vision transformer-equipped CNNs (VECNN) achieved strong three-way classification performance with notably high MCI sensitivity [20]. Combinations of residual depthwise separable 3D CNNs with Video Swin Transformers have achieved excellent AD classification performance, importantly demonstrating that 2D slice-based approaches substantially inflate accuracy compared to proper volumetric evaluation [21]. For MCI-to-AD progression prediction specifically, Vision Transformers applied to mid-sagittal slices achieved reasonable performance, though the use of single slices sacrifices spatial information present in full 3D volumes [28].

To address the limited availability of labeled neuroimaging data, self-supervised learning approaches have been employed. Masked Autoencoders (MAE) pretrained on diverse non-AD brain MRI datasets before fine-tuning on ADNI demonstrated effective transfer [29], and contrastive self-supervised learning achieved competitive balanced accuracy matching supervised baselines [30]. While promising, the application of these models to longitudinal, multi-timepoint MCI prediction remains limited.

While single-timepoint models have advanced the field, longitudinal structural MRI captures prognostic information beyond what baseline scans provide. This subsection examines the specific architectural design choices that determine how paired volumes are processed in longitudinal deep learning pipelines, focusing on three interrelated dimensions: the stage at which temporal inputs are merged, the weight-sharing strategy across parallel encoding streams, and the mathematical mechanisms used to fuse extracted features.

Early work on longitudinal MCI prediction explored early fusion, in which baseline and follow-up volumes are concatenated along the channel dimension before any feature extraction [31]. While straightforward, this forces initial layers to act simultaneously as spatial feature extractors and temporal comparators, making the network sensitive to registration errors. Late fusion, where final predictions are aggregated from independent pathways, avoids these issues but cannot model cross-temporal morphological interactions. The field has consequently converged on intermediate fusion [31, 32, 33]. In this paradigm, parallel encoding branches extract deep spatial representations independently before merging them at an intermediate network stage, allowing layers to learn spatiotemporal correlations from abstracted features rather than raw voxels.

Within intermediate fusion, true Siamese networks utilize identical branches with strictly shared weights, guaranteeing both volumes are projected into the same latent feature space [32]. Qiu et al. [32] demonstrated that this isolates morphological change effectively; any computed difference represents genuine anatomical change rather than encoder-specific artefacts. Shared weights also act as a structural regularizer by halving the parameter count. However, relaxing the Siamese constraint (“Twin” configurations) allows the baseline encoder to specialize in static structural vulnerabilities while the follow-up encoder adapts to active degenerative patterns, improving accuracy at the cost of higher overfitting risk [31].

Once spatial representations are extracted, the merge mechanism determines accessible temporal information. Element-wise subtraction directly isolates structural change magnitude, aligning with the clinical definition of neurodegeneration [32]. However, subtraction discards baseline context [31]. Feature concatenation preserves anatomical context but delegates temporal discovery to downstream dense layers, which struggle to align 3D spatial grids without geometric guidance [31]. To address this, recent architectures have adopted cross-attention. Chen et al. [33] developed LongFormer, implementing cross-attention directly on longitudinal pairs to resolve spatial misalignment. Zhang et al. [34] extended this with asymmetric, bidirectional cross-attention designs. Furthermore, adaptive temporal modulation has shown that explicitly conditioning features on the time interval between scans improves progression trajectory predictions [35].

The progression of these architectures reveals a clear trajectory from rigid arithmetic operations toward adaptive, attention-driven fusion. Subtraction isolates explicit change but discards context. Concatenation preserves bilateral information but lacks geometric alignment. Cross-attention dynamically aligns features but doesn’t provide explicit magnitude-of-change signals. No existing architecture simultaneously captures all three complementary views of the temporal relationship within a unified, learnable fusion mechanism. The architecture proposed in Section 4 addresses this gap.

### 3. Preprocessing

This section describes the data source and the standardised preprocessing pipeline applied to all structural MRI volumes prior to model training<sup>2</sup>. Rigorous preprocessing is essential in neuroimaging deep learning to ensure anatomical correspondence across subjects, remove non-brain tissue, and normalise intensity distributions that vary substantially between scanner acquisitions.

#### 3.1. Dataset

Data used in this study were obtained from the Alzheimer’s Disease Neuroimaging Initiative (ADNI) database ([adni.loni.usc.edu](http://adni.loni.usc.edu)). The ADNI was launched in 2003 as a public-private partnership, led by Principal Investigator Michael W. Weiner, MD. The primary goal of ADNI has been to test whether serial MRI, positron emission tomography, other biological markers, and clinical and neuropsychological assessment can be combined to measure the progression of MCI and early AD.

We selected subjects from the ADNI Complete 2-Year 3T cohort who had T1-weighted MRI scans at both baseline and 12-month follow-up visits, with clinical diagnosis of MCI at baseline and definitive conversion status available at the 36-month endpoint. Subjects were labelled as *progressive MCI* (pMCI; converter) if they received an AD diagnosis within 36 months, and *stable MCI* (sMCI; non-converter) otherwise. The final cohort comprised 319 MCI subjects (84 pMCI converters, 235 sMCI non-converters) contributing 529 longitudinal scan pairs across visit intervals of 6 to 24 months.

#### 3.2. Image Acquisition

All subjects were scanned on 3 Tesla MRI systems using standardised ADNI acquisition protocols. T1-weighted magnetisation-prepared rapid gradient echo (MPRAGE) sequences were acquired with the following nominal parameters: repetition time (TR)  $\approx$  2300 ms, echo time (TE)  $\approx$  2.98 ms, inversion time (TI)  $\approx$  900 ms, flip angle =  $9^\circ$ , and isotropic voxel resolution of approximately  $1.0 \times 1.0 \times 1.0$  mm<sup>3</sup>. Raw DICOM images were converted to NIfTI format using `dcm2nii` [36], applying BIDS-compliant naming conventions.

#### 3.3. Preprocessing Pipeline

Each T1-weighted volume underwent a standardised five-step preprocessing pipeline, summarised visually in Figure 1 and formalised in Algorithm 1. The pipeline transforms raw scanner-space volumes into spatially aligned, intensity-normalised, denoised volumes of fixed dimensions suitable for deep learning. The following subsections detail each step.

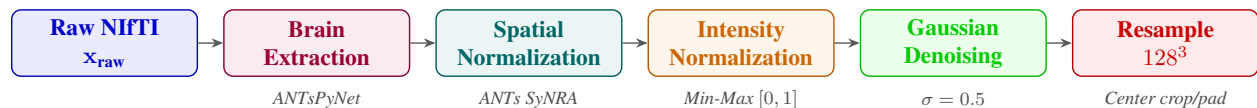


Figure 1: Overview of the five-step preprocessing pipeline. Each T1-weighted MRI volume is processed sequentially through brain extraction, spatial normalisation to a common template, intensity normalisation, Gaussian denoising, and resampling to a fixed  $128^3$  grid.

<sup>2</sup>Source code available at <https://github.com/amoayedikia/tafnet>.

---

**Algorithm 1** MRI Preprocessing Pipeline

---

**Require:** Raw T1-weighted volume  $\mathbf{x}_{\text{raw}} \in \mathbb{R}^{H \times W \times D}$ , MNI152 template  $\mathbf{T}$

**Ensure:** Preprocessed volume  $\mathbf{x} \in \mathbb{R}^{128 \times 128 \times 128}$ , intensities in  $[0, 1]$

**Step 1: Brain Extraction**

- 1:  $\mathbf{p} \leftarrow f_{\text{BE}}(\mathbf{x}_{\text{raw}}; \theta_{\text{BE}})$  ▷ Deep learning probability map,  $\mathbf{p} \in [0, 1]^{H \times W \times D}$
- 2:  $\mathbf{m} \leftarrow \mathbb{1}[\mathbf{p} > 0.5]$  ▷ Binary brain mask via thresholding
- 3:  $\mathbf{x}_{\text{brain}} \leftarrow \mathbf{x}_{\text{raw}} \odot \mathbf{m}$  ▷ Element-wise masking

**Step 2: Spatial Normalisation**

- 4:  $\phi^* \leftarrow \arg \min_{\phi} \mathcal{L}_{\text{sim}}(\mathbf{T}, \mathbf{x}_{\text{brain}} \circ \phi) + \lambda \mathcal{R}(\phi)$  ▷ SyNRA registration
- 5:  $\mathbf{x}_{\text{MNI}} \leftarrow \mathbf{x}_{\text{brain}} \circ \phi^*$  ▷ Apply optimal warp field

**Step 3: Intensity Normalisation**

- 6:  $\mathcal{B} \leftarrow \{(i, j, k) : \mathbf{x}_{\text{MNI}}(i, j, k) > 0\}$  ▷ Brain voxel indices
- 7:  $v_{\min} \leftarrow \min_{(i, j, k) \in \mathcal{B}} \mathbf{x}_{\text{MNI}}(i, j, k)$ ;  $v_{\max} \leftarrow \max_{(i, j, k) \in \mathcal{B}} \mathbf{x}_{\text{MNI}}(i, j, k)$
- 8:  $\mathbf{x}_{\text{norm}}(i, j, k) \leftarrow \begin{cases} \frac{\mathbf{x}_{\text{MNI}}(i, j, k) - v_{\min}}{v_{\max} - v_{\min}} & \text{if } (i, j, k) \in \mathcal{B} \\ 0 & \text{otherwise} \end{cases}$

**Step 4: Gaussian Denoising**

- 9:  $\mathbf{x}_{\text{smooth}} \leftarrow G_{\sigma} * \mathbf{x}_{\text{norm}}$  ▷ 3D convolution with Gaussian kernel,  $\sigma = 0.5$
- 10:  $\mathbf{x}_{\text{smooth}}(i, j, k) \leftarrow 0 \quad \forall (i, j, k) \notin \mathcal{B}$  ▷ Preserve background

**Step 5: Spatial Resampling**

- 11:  $\mathbf{x} \leftarrow \text{CENTERCROPPAD}(\mathbf{x}_{\text{smooth}}, 128^3)$  ▷ Center crop or zero-pad to target size
  - 12: **return**  $\mathbf{x}$
- 

### 3.3.1. Step 1: Brain Extraction

Non-brain tissue—including skull, dura mater, and extracranial soft tissue—must be removed to prevent the model from learning spurious anatomical correlates unrelated to neurodegeneration. We employed ANTsPyNet’s deep learning-based brain extraction model [37], which applies a pretrained 3D U-Net architecture to generate a voxel-wise probability map  $\mathbf{p} \in [0, 1]^{H \times W \times D}$  indicating the likelihood of each voxel belonging to brain parenchyma:

$$\mathbf{p} = f_{\text{BE}}(\mathbf{x}_{\text{raw}}; \theta_{\text{BE}}), \quad (1)$$

where  $f_{\text{BE}}$  denotes the pretrained extraction network with frozen parameters  $\theta_{\text{BE}}$ . The binary brain mask  $\mathbf{m}$  is obtained by thresholding the probability map at  $\tau = 0.5$ :

$$\mathbf{m}(i, j, k) = \mathbb{1}[\mathbf{p}(i, j, k) > \tau], \quad (2)$$

and the skull-stripped brain volume is computed via element-wise multiplication:

$$\mathbf{x}_{\text{brain}} = \mathbf{x}_{\text{raw}} \odot \mathbf{m}. \quad (3)$$

### 3.3.2. Step 2: Spatial Normalisation

To enable voxel-wise comparisons across subjects, all brain-extracted volumes were registered to the MNI152 standard-space template using the Advanced Normalisation Tools (ANTs) software [38]. We employed the SyNRA registration algorithm, which combines an initial rigid alignment followed by affine

transformation and symmetric diffeomorphic normalisation (SyN). The optimal transformation  $\phi^*$  is obtained by solving:

$$\phi^* = \arg \min_{\phi} \mathcal{L}_{\text{sim}}(\mathbf{T}, \mathbf{x}_{\text{brain}} \circ \phi) + \lambda \mathcal{R}(\phi), \quad (4)$$

where  $\mathbf{T}$  denotes the MNI152 template,  $\circ$  denotes spatial transformation,  $\mathcal{L}_{\text{sim}}$  is a similarity metric (cross-correlation), and  $\mathcal{R}(\phi)$  is a regularisation term enforcing smooth, invertible deformations with weight  $\lambda$ . The registered volume is then computed as:

$$\mathbf{x}_{\text{MNI}} = \mathbf{x}_{\text{brain}} \circ \phi^*. \quad (5)$$

The SyNRA variant was selected as a compromise between registration accuracy and computational efficiency, requiring approximately 90–120 seconds per volume on a single GPU compared to >300 seconds for full SyN [38]. After registration, all volumes occupy a common anatomical coordinate system with consistent spatial dimensions, enabling direct comparison of homologous brain regions across subjects and timepoints.

### 3.3.3. Step 3: Intensity Normalisation

T1-weighted MRI intensities vary substantially across scanners, acquisition protocols, and individual subjects due to differences in receiver coil sensitivity, RF calibration, and tissue relaxation properties. To ensure comparable input distributions for the neural network, we applied min-max normalisation restricted to brain voxels. Let  $\mathcal{B} = \{(i, j, k) : \mathbf{x}_{\text{MNI}}(i, j, k) > 0\}$  denote the set of non-zero brain voxels. The normalised intensity at each voxel is:

$$\mathbf{x}_{\text{norm}}(i, j, k) = \begin{cases} \frac{\mathbf{x}_{\text{MNI}}(i, j, k) - v_{\min}}{v_{\max} - v_{\min}} & \text{if } (i, j, k) \in \mathcal{B}, \\ 0 & \text{otherwise,} \end{cases} \quad (6)$$

where  $v_{\min} = \min_{(i,j,k) \in \mathcal{B}} \mathbf{x}_{\text{MNI}}(i, j, k)$  and  $v_{\max} = \max_{(i,j,k) \in \mathcal{B}} \mathbf{x}_{\text{MNI}}(i, j, k)$  are computed exclusively over brain tissue. This formulation maps brain intensities to the unit interval  $[0, 1]$  while preserving the zero-valued background, ensuring that the network receives consistent input magnitudes regardless of the original scanner dynamic range.

### 3.3.4. Step 4: Gaussian Denoising

MRI acquisitions inherently contain thermal noise from the receiver coil electronics, which manifests as high-frequency intensity fluctuations. To reduce noise while preserving anatomically meaningful edges, we applied isotropic Gaussian smoothing with a small kernel width. The smoothed volume is obtained via 3D convolution:

$$\mathbf{x}_{\text{smooth}} = G_{\sigma} * \mathbf{x}_{\text{norm}}, \quad (7)$$

where  $G_{\sigma}$  is a 3D Gaussian kernel with standard deviation  $\sigma = 0.5$  voxels, and  $*$  denotes convolution. The Gaussian kernel is defined as:

$$G_{\sigma}(i, j, k) = \frac{1}{(2\pi\sigma^2)^{3/2}} \exp\left(-\frac{i^2 + j^2 + k^2}{2\sigma^2}\right). \quad (8)$$

The choice of  $\sigma = 0.5$  represents a conservative smoothing that suppresses high-frequency noise while preserving fine anatomical boundaries critical for detecting subtle atrophy patterns. After smoothing, background voxels are reset to zero to maintain the brain mask boundary:

$$\mathbf{x}_{\text{smooth}}(i, j, k) \leftarrow 0 \quad \forall (i, j, k) \notin \mathcal{B}. \quad (9)$$

To quantify noise reduction, we computed a gradient-based noise estimate before and after denoising:

$$\hat{\sigma}_e = \sqrt{\frac{1}{3} (\text{Var}(\nabla_x \mathbf{x}) + \text{Var}(\nabla_y \mathbf{x}) + \text{Var}(\nabla_z \mathbf{x}))}, \quad (10)$$

where  $\nabla_x, \nabla_y, \nabla_z$  denote finite differences along each axis. Across the cohort, the mean noise estimate decreased from  $0.042 \pm 0.008$  before denoising to  $0.037 \pm 0.006$  after, representing an 11.9% reduction.

### 3.3.5. Step 5: Spatial Resampling

Although registration to MNI152 standardises anatomical alignment, the resulting volumes may have slightly varying dimensions depending on the original field of view. To ensure uniform input tensor dimensions for batch processing, all volumes were resampled to a fixed  $128 \times 128 \times 128$  grid via center cropping (if oversized) or zero-padding (if undersized):

$$\mathbf{x} = \text{CENTERCROPPAD}(\mathbf{x}_{\text{smooth}}, 128^3). \quad (11)$$

The center cropping and padding operation is defined as follows. Let  $\mathbf{s} = (s_1, s_2, s_3)$  denote the current spatial dimensions and  $\mathbf{t} = (128, 128, 128)$  the target dimensions. For each axis  $a \in \{1, 2, 3\}$ :

- If  $s_a > t_a$ : extract the central  $t_a$  voxels, discarding  $\lfloor (s_a - t_a)/2 \rfloor$  voxels from each end.
- If  $s_a < t_a$ : pad with  $\lfloor (t_a - s_a)/2 \rfloor$  zeros before and  $\lceil (t_a - s_a)/2 \rceil$  zeros after.

This symmetric operation preserves the brain centroid at the volume center, ensuring consistent spatial alignment of key anatomical landmarks across all subjects. The final preprocessed volume  $\mathbf{x} \in \mathbb{R}^{128 \times 128 \times 128}$  with voxel intensities in  $[0, 1]$  serves as input to the TAF-Net architecture described in Section 4.

Figure 2 presents orthogonal slices through a representative preprocessed volume, illustrating the output quality achieved by the five-stage pipeline. The axial view at the level of the lateral ventricles demonstrates clear grey-white matter contrast and well-defined ventricular boundaries, both critical for detecting the ventricular enlargement characteristic of AD-related atrophy. The coronal section through the temporal lobes reveals the hippocampal formations bilaterally, regions of particular importance given their established role as early sites of neurodegeneration in the Alzheimer’s continuum. The sagittal midline slice displays the corpus callosum and cerebellar structures with preserved anatomical detail, confirming that the registration and resampling operations maintain structural integrity across the entire brain volume.

Several qualitative features merit attention. The uniform background intensity surrounding the brain parenchyma confirms successful skull stripping, with no residual extracranial tissue that could confound subsequent feature extraction. The consistent intensity range across tissue types reflects the effectiveness of the min-max normalisation procedure, which standardises the input distribution regardless of original scanner characteristics. The subtle smoothing introduced by the Gaussian denoising step is visually imperceptible at this display resolution, indicating that the conservative kernel width preserves anatomically meaningful boundaries while suppressing acquisition noise. Finally, the symmetric positioning of the brain within the volume grid confirms proper centring during the resampling operation, ensuring that homologous anatomical structures occupy consistent spatial locations across the cohort.

These visual characteristics are representative of the full dataset following quality control procedures. All 529 preprocessed scan pairs exhibited comparable image quality, with clear anatomical delineation and standardised spatial positioning suitable for input to the deep learning architecture.

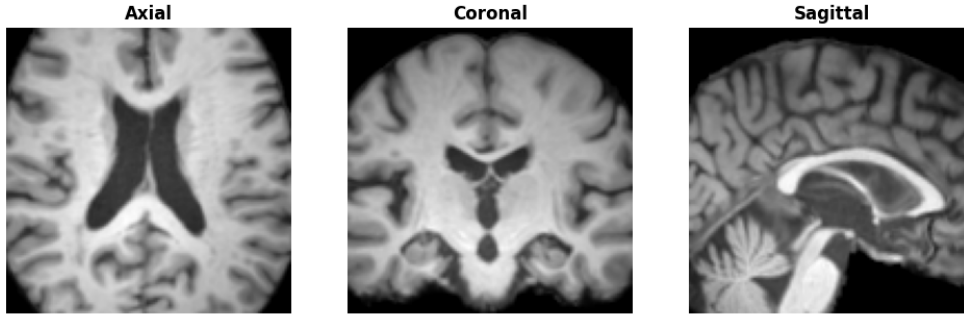


Figure 2: Representative preprocessed MRI volume from a participant in the study cohort (Subject 002\_S\_0413). The three orthogonal views display central slices through the axial, coronal, and sagittal planes following completion of the five-stage preprocessing pipeline. The final volume occupies a  $128 \times 128 \times 128$  voxel grid with intensity values normalised to the  $[0, 1]$  range. Note the clear tissue contrast, well-defined anatomical boundaries, and absence of extracranial structures following brain extraction and spatial normalisation to MNI152 standard space.

### 3.4. Data Augmentation

To improve model generalisation and mitigate overfitting on the limited training cohort, we applied stochastic data augmentation during training. Each volume, along with its paired follow-up when applicable, underwent a series of geometric and intensity transformations with independent random sampling at each training epoch.

The first transformation consisted of random horizontal reflection, applied with probability  $p = 0.5$ . Due to the approximate bilateral symmetry of the human brain, this left-right flipping operation effectively doubles the training set size without introducing anatomically implausible configurations. The second transformation involved small-angle rotations uniformly sampled from the range  $[-5^\circ, +5^\circ]$  about each of the three principal axes, with the rotated volume reconstructed via trilinear interpolation. These modest angular perturbations simulate the minor head positioning variations that naturally occur between scanning sessions, thereby encouraging the network to learn rotation-invariant representations. The third transformation applied multiplicative intensity scaling with factors uniformly sampled from the interval  $[0.95, 1.05]$ , simulating the gain variations that arise from differences in receiver coil sensitivity and scanner calibration across acquisition sites.

A critical consideration for longitudinal analysis is the preservation of temporal correspondence between paired scans. To maintain the integrity of the baseline-to-follow-up relationship, all geometric transformations were applied identically to both volumes within a longitudinal pair using the same randomly sampled parameters. This synchronised augmentation strategy ensures that any structural differences between timepoints reflect genuine anatomical change rather than artefacts introduced by inconsistent spatial transformations. No augmentation was applied during validation or testing to ensure unbiased performance estimation.

### 3.5. Quality Control

All preprocessed volumes were subjected to a series of automated quality control checks prior to inclusion in the final dataset. The first criterion verified that each output volume possessed the expected spatial dimensions of  $128 \times 128 \times 128$  voxels, confirming successful completion of the resampling stage. The second criterion examined the intensity distribution, requiring that all voxel values fall within the normalised range  $[0, 1]$  as specified by the min-max scaling procedure. The third criterion assessed brain extraction quality by counting the number of non-zero voxels within each volume, with a minimum threshold of 100,000 voxels,

corresponding to approximately 12% of the total volume capacity. Volumes falling below this threshold indicated potential failure of the skull-stripping or registration algorithms, warranting further investigation.

Scans failing any of these automated criteria were flagged for manual visual inspection by a trained operator. The manual review process involved examination of the preprocessed volume alongside the original raw scan to identify the source of quality degradation. Common failure modes included severe subject motion during acquisition, which manifested as blurring or ghosting artefacts, and registration failures characterised by gross misalignment with the MNI152 template. Of the initial cohort, a small number of scans required manual inspection, and those exhibiting irrecoverable artefacts were excluded from subsequent analysis. The quality control pipeline ensured that only volumes meeting stringent standards for spatial alignment, intensity normalisation, and anatomical integrity were included in the final dataset used for model training and evaluation.

## 4. Proposed Method

This section presents the Temporal Attention Fusion Network (TAF-Net), a hybrid CNN-Transformer architecture designed to predict 3-year MCI-to-AD conversion from paired longitudinal structural MRI scans. The architecture comprises three stages: a Siamese 3D CNN encoder with shared weights for spatial feature extraction, a Temporal Fusion Module containing three complementary fusion branches governed by an adaptive gating mechanism, and a classification head. Figure 3 illustrates the complete architecture, provides the corresponding procedural summary of the end-to-end forward pass: given a baseline–follow-up MRI pair, the shared encoder extracts bottleneck features, the Temporal Fusion Module merges them into a unified temporal representation, and the classification head produces a conversion probability. Sections 4.1–4.3 detail each of these stages in turn, and Section 4.4 describes the interpretability mechanisms.

### 4.1. Stage 1: Siamese 3D CNN Encoder

Let  $\mathbf{x}_{\text{BL}} \in \mathbb{R}^{1 \times 128 \times 128 \times 128}$  and  $\mathbf{x}_{\text{M12}} \in \mathbb{R}^{1 \times 128 \times 128 \times 128}$  denote the preprocessed baseline and 12-month follow-up T1-weighted MRI volumes, respectively. A shared encoder  $E$  with parameters  $\theta$  extracts deep spatial feature maps from each timepoint independently:

$$\mathbf{f}_{\text{BL}} = E(\mathbf{x}_{\text{BL}}; \theta), \quad \mathbf{f}_{\text{M12}} = E(\mathbf{x}_{\text{M12}}; \theta), \quad \mathbf{f} \in \mathbb{R}^{128 \times 8 \times 8 \times 8}. \quad (12)$$

The encoder follows a five-block 3D convolutional architecture with channel progression  $16 \rightarrow 32 \rightarrow 64 \rightarrow 128 \rightarrow 128$ , whose per-block computation is detailed in Algorithm 2. Each block comprises two sequential  $3^3$  convolution layers with batch normalisation and LeakyReLU activation (Algorithm 2, lines 4–5), followed by  $2^3$  max-pooling applied after the first four blocks (line 10), progressively reducing spatial dimensions from  $128^3$  to  $8^3$ . Dynamic Contextual Channel Attention (DCCA) modules are applied after each encoder block to recalibrate channel-wise feature responses: a contextual encoding pathway generates channel weights  $\mathbf{w}_i^c$  via global average pooling and a fully connected layer (lines 6–7), which are then applied through element-wise multiplication to suppress uninformative channels and amplify diagnostically relevant ones.

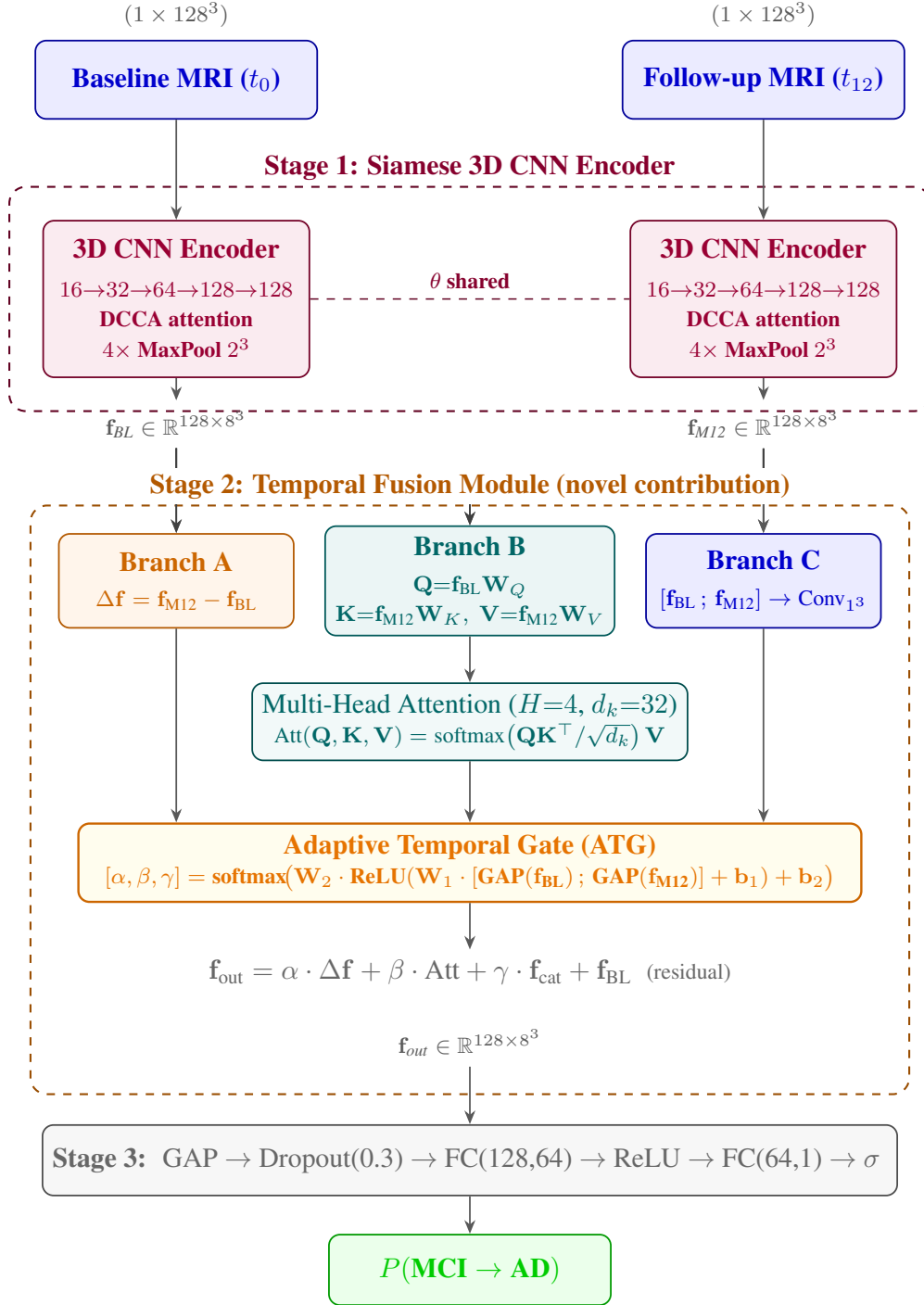


Figure 3: Architecture of TAF-Net. *Stage 1*: A Siamese 3D CNN encoder with shared parameters  $\theta$  extracts bottleneck feature maps from baseline and 12-month follow-up MRI volumes. *Stage 2*: The Temporal Fusion Module processes the paired features through three complementary branches—temporal difference, cross-temporal attention, and channel concatenation—whose outputs are combined via a learned Adaptive Temporal Gate (ATG) with a baseline residual connection. *Notation*:  $[\mathbf{a}; \mathbf{b}]$  denotes concatenation along the channel axis, and  $\mathbf{f}_{cat} = \text{Conv}_{13}([\mathbf{f}_{BL}; \mathbf{f}_{M12}])$  is the output of Branch C. The projection matrices  $\mathbf{W}_Q, \mathbf{W}_K, \mathbf{W}_V$  in Branch B are learned (see Algorithm 3, lines 4–5). *Stage 3*: A lightweight classification head produces the conversion probability. Dashed borders indicate logical groupings.

---

**Algorithm 2** Siamese 3D CNN Encoder

---

**Require:** Input volume  $\mathbf{x} \in \mathbb{R}^{1 \times 128 \times 128 \times 128}$

**Ensure:** Bottleneck features  $\mathbf{f} \in \mathbb{R}^{128 \times 8 \times 8 \times 8}$ , skip features  $\{\mathbf{s}_i\}_{i=1}^5$

```
1:  $C \leftarrow [16, 32, 64, 128, 128]$  ▷ Channel progression
2:  $\mathbf{h}_0 \leftarrow \mathbf{x}$ 
3: for  $i = 1$  to 5 do
    % Double convolution block
4:    $\mathbf{h}_i \leftarrow \text{LeakyReLU}(\text{BN}(\text{Conv3D}_{3^3}(\mathbf{h}_{i-1}, C[i])))$ 
5:    $\mathbf{h}_i \leftarrow \text{LeakyReLU}(\text{BN}(\text{Conv3D}_{3^3}(\mathbf{h}_i, C[i])))$ 
    % Dynamic Contextual Channel Attention
6:    $\mathbf{w}_i^c \leftarrow \sigma(\text{FC}(\text{GAP}(\text{ReLU}(\text{Conv3D}_{3^3}(\text{ReLU}(\text{Conv3D}_{3^3}(\mathbf{h}_i)))))))$ 
7:    $\mathbf{h}_i \leftarrow \mathbf{h}_i \odot \mathbf{w}_i^c$  ▷ Channel-wise recalibration
8:    $\mathbf{s}_i \leftarrow \mathbf{h}_i$  ▷ Store skip connection
9:   if  $i \leq 4$  then
10:     $\mathbf{h}_i \leftarrow \text{MaxPool3D}_{2^3}(\mathbf{h}_i)$  ▷ Downsample spatial dims by 2
11:   end if
12: end for
13:  $\mathbf{f} \leftarrow \mathbf{h}_5$  ▷ Bottleneck:  $128 \times 8 \times 8 \times 8$ 
14: return  $\mathbf{f}, \{\mathbf{s}_i\}_{i=1}^5$ 
```

---

The decision to employ a Siamese architecture with shared weights, rather than an independent-weight dual-stream configuration, is motivated by the small paired cohort available for this study. While independent weights have been shown to outperform shared weights on larger cohorts by enabling asymmetric baseline and follow-up feature specialisation [31], doubling the encoder parameters on a small dataset presents severe overfitting risk. Shared weights enforce a strict metric space in which any computed difference  $\mathbf{f}_{M12} - \mathbf{f}_{BL}$  represents true morphological change rather than encoder-specific artefacts [32], while simultaneously halving the encoder parameter count. Recent work on stochastic Siamese pretraining has validated that shared-weight architectures can match independent-weight performance when asymmetry is injected at the fusion stage rather than the encoder level [35], precisely the strategy adopted by our Temporal Fusion Module.

#### 4.2. Stage 2: Temporal Fusion Module

The Temporal Fusion Module (TFM) is the core novel contribution of this work. Existing longitudinal architectures employ a single fusion strategy—subtraction [32], concatenation [31], or cross-attention [33]—each with demonstrated limitations (Section 1). The TFM addresses these limitations through three complementary fusion branches whose outputs are combined via a learned adaptive gating mechanism. Algorithm 3 provides the complete procedural specification: line 1 computes the temporal difference (Branch A), lines 2–10 perform cross-temporal attention (Branch B), line 11 applies concatenation with convolution (Branch C), and lines 12–14 merge the three branch outputs through the Adaptive Temporal Gate and a residual connection. The following subsections describe each component in detail.

---

**Algorithm 3** Temporal Fusion Module (TFM)

---

**Require:** Baseline features  $\mathbf{f}_{\text{BL}} \in \mathbb{R}^{128 \times 8^3}$ , follow-up features  $\mathbf{f}_{\text{M12}} \in \mathbb{R}^{128 \times 8^3}$

**Ensure:** Fused temporal features  $\mathbf{f}_{\text{out}} \in \mathbb{R}^{128 \times 8^3}$

**Branch A: Temporal Difference**

1:  $\Delta \mathbf{f} \leftarrow \mathbf{f}_{\text{M12}} - \mathbf{f}_{\text{BL}}$  ▷ Explicit structural change

**Branch B: Cross-Temporal Attention**

2:  $\tilde{\mathbf{f}}_{\text{BL}} \leftarrow \text{Reshape}(\mathbf{f}_{\text{BL}})$  ▷  $(B, 128, 8, 8, 8) \rightarrow (B, 512, 128)$

3:  $\tilde{\mathbf{f}}_{\text{M12}} \leftarrow \text{Reshape}(\mathbf{f}_{\text{M12}})$  ▷  $512 = 8^3$  spatial tokens

4:  $\mathbf{Q} \leftarrow \tilde{\mathbf{f}}_{\text{BL}} \mathbf{W}_Q$  ▷ Queries from baseline

5:  $\mathbf{K} \leftarrow \tilde{\mathbf{f}}_{\text{M12}} \mathbf{W}_K; \mathbf{V} \leftarrow \tilde{\mathbf{f}}_{\text{M12}} \mathbf{W}_V$  ▷ Keys/values from follow-up

6: **for**  $h = 1$  **to**  $H$  **do** ▷  $H = 4$  attention heads

7:  $\mathbf{A}_h \leftarrow \text{softmax}(\mathbf{Q}_h \mathbf{K}_h^\top / \sqrt{d_k})$  ▷  $d_k = 32; \mathbf{A}_h \in \mathbb{R}^{512 \times 512}$

8:  $\mathbf{O}_h \leftarrow \mathbf{A}_h \mathbf{V}_h$

9: **end for**

10:  $\text{Att} \leftarrow \text{Reshape}([\mathbf{O}_1; \dots; \mathbf{O}_H] \cdot \mathbf{W}_O)$  ▷ Back to  $\mathbb{R}^{128 \times 8^3}$

**Branch C: Concatenation + Convolution**

11:  $\mathbf{f}_{\text{cat}} \leftarrow \text{Conv3D}_{13}([\mathbf{f}_{\text{BL}}; \mathbf{f}_{\text{M12}}])$  ▷  $\mathbb{R}^{256 \times 8^3} \rightarrow \mathbb{R}^{128 \times 8^3}$

**Adaptive Temporal Gate**

12:  $\alpha, \beta, \gamma \leftarrow \text{ATG}(\mathbf{f}_{\text{BL}}, \mathbf{f}_{\text{M12}})$  ▷ Algorithm 4

13:  $\mathbf{f}_{\text{fused}} \leftarrow \alpha \cdot \Delta \mathbf{f} + \beta \cdot \text{Att} + \gamma \cdot \mathbf{f}_{\text{cat}}$  ▷ Weighted mixture

14:  $\mathbf{f}_{\text{out}} \leftarrow \mathbf{f}_{\text{fused}} + \mathbf{f}_{\text{BL}}$  ▷ Baseline residual connection

15: **return**  $\mathbf{f}_{\text{out}}$

---

#### 4.2.1. Branch A: Temporal Difference

The element-wise difference (Algorithm 3, line 1) directly isolates the magnitude and direction of structural change between timepoints:

$$\Delta \mathbf{f} = \mathbf{f}_{\text{M12}} - \mathbf{f}_{\text{BL}} \in \mathbb{R}^{128 \times 8 \times 8 \times 8}. \quad (13)$$

Because the shared encoder projects both volumes into an identical latent space, positive and negative activations in  $\Delta \mathbf{f}$  correspond directly to regional volume loss and expansion, respectively. This branch is maximally interpretable—the resulting feature map represents what changed—and aligns with the clinical definition of neurodegeneration as progressive atrophy. However, subtraction erases baseline context: a patient with a naturally small hippocampus experiencing minor atrophy may be at higher conversion risk than one with a large hippocampus experiencing the same absolute loss, yet both produce identical difference vectors [31].

#### 4.2.2. Branch B: Cross-Temporal Attention

To capture non-linear, region-to-region temporal correlations, the bottleneck features are reshaped to sequences of spatial tokens  $\mathbf{f} \in \mathbb{R}^{B \times 512 \times 128}$ , where  $512 = 8^3$  spatial positions serve as the sequence length and 128 channels form the token dimension (Algorithm 3, lines 2–3). Multi-head cross-attention is then computed with the baseline features as queries and the follow-up features providing keys and values

(lines 4–10):

$$\mathbf{Q} = \mathbf{f}_{\text{BL}} \mathbf{W}_Q, \quad \mathbf{K} = \mathbf{f}_{\text{M12}} \mathbf{W}_K, \quad \mathbf{V} = \mathbf{f}_{\text{M12}} \mathbf{W}_V, \quad (14)$$

$$\text{Att}(\mathbf{Q}, \mathbf{K}, \mathbf{V}) = \text{softmax}\left(\frac{\mathbf{Q}\mathbf{K}^\top}{\sqrt{d_k}}\right) \mathbf{V}, \quad (15)$$

with  $H = 4$  attention heads and head dimension  $d_k = 128/4 = 32$ . The attention matrix  $\mathbf{A} \in \mathbb{R}^{512 \times 512}$  is computationally feasible at the  $8^3$  bottleneck resolution ( $\sim 1$  MB per sample). By querying the baseline against the follow-up, each spatial position in the baseline “asks” every position in the follow-up how it has changed, allowing the network to contextualise local atrophy within the global structural trajectory. This addresses the finding that temporal progression in the brain is a spatially interconnected cascade—a change in hippocampal volume is mathematically contextualised by simultaneous cortical thinning, a dependency that subtraction alone cannot represent [33]. The attended output is reshaped back to  $\mathbb{R}^{128 \times 8 \times 8 \times 8}$ .

#### 4.2.3. Branch C: Concatenation with Convolution

Full-state preservation is achieved through channel concatenation followed by learned dimensionality reduction (Algorithm 3, line 11):

$$\mathbf{f}_{\text{cat}} = \text{Conv3D}_{1^3}([\mathbf{f}_{\text{BL}}; \mathbf{f}_{\text{M12}}]) : \mathbb{R}^{256 \times 8^3} \rightarrow \mathbb{R}^{128 \times 8^3}, \quad (16)$$

where  $[\cdot; \cdot]$  denotes concatenation along the channel axis. Unlike the approach of Martínez-Murcia et al. [31], which flattened features before concatenation and thereby destroyed spatial topology, this branch preserves the 3D structure via a  $1 \times 1 \times 1$  convolution. The full bilateral context of both timepoints is retained, enabling the downstream gate to leverage baseline vulnerability alongside follow-up state when neither explicit change nor correlative attention alone is sufficient.

#### 4.2.4. Adaptive Temporal Gate

The three branch outputs represent complementary views of the temporal relationship: explicit change ( $\Delta\mathbf{f}$ ), correlative alignment (Att), and full bilateral context ( $\mathbf{f}_{\text{cat}}$ ). Rather than fixing their relative contribution, an Adaptive Temporal Gate (ATG) learns patient-specific mixture weights, as formalised in Algorithm 4. The procedure begins by compressing the full spatial feature maps to compact global descriptors via global average pooling (Algorithm 4, lines 1–2), then concatenating the two 128-dimensional descriptors into a single conditioning vector  $\mathbf{g} \in \mathbb{R}^{256}$  (line 3). A two-layer MLP maps this vector through a hidden dimension of 64 to three raw logits (lines 4–5), and a softmax activation produces the final gating coefficients (line 6):

$$\mathbf{g} = [\text{GAP}(\mathbf{f}_{\text{BL}}); \text{GAP}(\mathbf{f}_{\text{M12}})] \in \mathbb{R}^{256}, \quad (17)$$

$$[\alpha, \beta, \gamma] = \text{softmax}(\mathbf{W}_2 \cdot \text{ReLU}(\mathbf{W}_1 \mathbf{g} + \mathbf{b}_1) + \mathbf{b}_2), \quad (18)$$

$$\mathbf{f}_{\text{fused}} = \alpha \cdot \Delta\mathbf{f} + \beta \cdot \text{Att} + \gamma \cdot \mathbf{f}_{\text{cat}}. \quad (19)$$

The softmax constraint ensures  $\alpha + \beta + \gamma = 1$ , creating an interpretable mixture in which each coefficient directly reflects the relative importance of its corresponding fusion strategy for a given patient. A baseline residual connection then preserves static anatomical context, corresponding to Algorithm 3, line 14:

$$\mathbf{f}_{\text{out}} = \mathbf{f}_{\text{fused}} + \mathbf{f}_{\text{BL}}. \quad (20)$$

The gate mechanism is inspired by attention-guided feature selection approaches [39], extended here to operate over fusion strategies rather than spatial regions. Importantly, the entire ATG pathway (Algorithm 4)

adds only  $\sim 16.6\text{K}$  parameters ( $256 \rightarrow 64 \rightarrow 3$ ), making it negligible relative to the encoder while providing both adaptive fusion and a built-in interpretability channel through the gate coefficients.

---

**Algorithm 4** Adaptive Temporal Gate (ATG)

---

**Require:** Baseline features  $\mathbf{f}_{\text{BL}} \in \mathbb{R}^{128 \times 8^3}$ , follow-up features  $\mathbf{f}_{\text{M12}} \in \mathbb{R}^{128 \times 8^3}$

**Ensure:** Gate coefficients  $\alpha, \beta, \gamma \in [0, 1]$  with  $\alpha + \beta + \gamma = 1$

*% Compress spatial dimensions to global descriptors*

1:  $\mathbf{z}_{\text{BL}} \leftarrow \text{GAP}(\mathbf{f}_{\text{BL}})$

$\triangleright \mathbb{R}^{128 \times 8^3} \rightarrow \mathbb{R}^{128}$

2:  $\mathbf{z}_{\text{M12}} \leftarrow \text{GAP}(\mathbf{f}_{\text{M12}})$

$\triangleright \mathbb{R}^{128 \times 8^3} \rightarrow \mathbb{R}^{128}$

*% Concatenate global descriptors from both timepoints*

3:  $\mathbf{g} \leftarrow [\mathbf{z}_{\text{BL}} ; \mathbf{z}_{\text{M12}}]$

$\triangleright \mathbf{g} \in \mathbb{R}^{256}$

*% Two-layer MLP:  $256 \rightarrow 64 \rightarrow 3$*

4:  $\mathbf{g}' \leftarrow \text{ReLU}(\mathbf{W}_1 \cdot \mathbf{g} + \mathbf{b}_1)$

$\triangleright$  Hidden layer,  $\mathbf{g}' \in \mathbb{R}^{64}$

5:  $\mathbf{l} \leftarrow \mathbf{W}_2 \cdot \mathbf{g}' + \mathbf{b}_2$

$\triangleright$  Logits,  $\mathbf{l} \in \mathbb{R}^3$

*% Softmax ensures interpretable, normalised mixture*

6:  $[\alpha, \beta, \gamma] \leftarrow \text{softmax}(\mathbf{l})$

$\triangleright \alpha$ : difference,  $\beta$ : attention,  $\gamma$ : concat

7: **return**  $\alpha, \beta, \gamma$

---

### 4.3. Stage 3: Classification Head

The fused output  $\mathbf{f}_{\text{out}}$  passes through global average pooling to produce a 128-dimensional feature vector, followed by a two-layer fully connected network with interleaved dropout, as specified in lines 4–6 of Algorithm 5:

$$P(\text{conversion}) = \sigma(\mathbf{W}_4 \cdot \text{ReLU}(\mathbf{W}_3 \cdot \text{GAP}(\mathbf{f}_{\text{out}}) + \mathbf{b}_3) + \mathbf{b}_4), \quad (21)$$

with intermediate dimension 64, dropout rate 0.3 applied before each linear layer, and  $\sigma$  denoting the sigmoid function. Training uses binary cross-entropy loss with the AdamW optimiser. The total parameter count of TAF-Net is approximately 1.39M, of which the Temporal Fusion Module contributes only  $\sim 181\text{K}$  (15% overhead relative to the baseline-only model).

### 4.4. Interpretability

TAF-Net provides two complementary interpretability mechanisms, constituting the third stated contribution of this study. Both are extracted during inference via the procedure specified in Algorithm 5.

The first mechanism leverages the cross-attention weight matrix  $\mathbf{A} \in \mathbb{R}^{512 \times 512}$  from Branch B. As detailed in Algorithm 5, lines 2–7, the per-head attention matrices are first averaged across all  $H$  heads to produce a single  $\bar{\mathbf{A}}$  (line 3), then the total attention received at each query position is computed by column-wise summation (line 4). The resulting 512-dimensional vector is reshaped to the  $8^3$  bottleneck grid (line 5) and upsampled to the original MRI resolution via trilinear interpolation (line 6). The normalised map can be overlaid on the MNI152 template for direct anatomical interpretation, highlighting which brain regions the model considers most informative for temporal comparison.

The second mechanism exploits the gate coefficients  $(\alpha, \beta, \gamma)$  produced by the ATG for each patient (Algorithm 5, lines 8–9, which invokes Algorithm 4). These coefficients provide a categorical interpretability signal: patients dominated by  $\alpha$  exhibit clear, localised atrophy patterns best captured by explicit difference; patients dominated by  $\beta$  show distributed, correlated structural changes requiring cross-attention; and patients

dominated by  $\gamma$  may require full bilateral context for prediction. Because the softmax constraint ensures the coefficients sum to unity, they can be directly visualised as a ternary composition for each patient and correlated with clinical variables such as MMSE decline rate and APOE genotype status for secondary analysis.

---

**Algorithm 5** Interpretability: Attention Map and Gate Extraction

---

**Require:** Trained TAF-Net with parameters  $\Theta_{\text{best}}$ , test subject  $(\mathbf{x}_{\text{BL}}, \mathbf{x}_{\text{M12}})$

**Ensure:** Spatial attention map  $\mathbf{M}_{\text{attn}} \in \mathbb{R}^{128^3}$ , gate profile  $(\alpha, \beta, \gamma)$

*% Forward pass with intermediate storage*

1:  $\mathbf{f}_{\text{BL}}, \mathbf{f}_{\text{M12}} \leftarrow E(\mathbf{x}_{\text{BL}}; \theta), E(\mathbf{x}_{\text{M12}}; \theta)$

**(a) Cross-Attention Map Extraction**

2: Compute  $\mathbf{A}_h \in \mathbb{R}^{512 \times 512}$  for each head  $h$

▷ From Algorithm 3, line 7

3:  $\bar{\mathbf{A}} \leftarrow \frac{1}{H} \sum_{h=1}^H \mathbf{A}_h$

▷ Head-averaged attention

4:  $\mathbf{a} \leftarrow \sum_{j=1}^{512} \bar{\mathbf{A}}_{:,j}$

▷ Sum received attention per query,  $\mathbf{a} \in \mathbb{R}^{512}$

5:  $\mathbf{M}_{8^3} \leftarrow \text{Reshape}(\mathbf{a})$

▷  $\mathbb{R}^{512} \rightarrow \mathbb{R}^{8 \times 8 \times 8}$

6:  $\mathbf{M}_{\text{attn}} \leftarrow \text{Upsample}(\mathbf{M}_{8^3}, 128^3)$

▷ Trilinear interpolation

7: Normalise  $\mathbf{M}_{\text{attn}}$  to  $[0, 1]$  for overlay on MNI152 template

**(b) Gate Coefficient Extraction**

8:  $\alpha, \beta, \gamma \leftarrow \text{ATG}(\mathbf{f}_{\text{BL}}, \mathbf{f}_{\text{M12}})$

▷ Algorithm 4

9: Record  $(\alpha, \beta, \gamma)$  alongside clinical variables for correlation analysis

10: **return**  $\mathbf{M}_{\text{attn}}, (\alpha, \beta, \gamma)$

---

## 5. Experimental Setup

This section describes the evaluation protocol, benchmark methods, and training strategy employed to assess the proposed TAFNet architecture. All implementation details are specified to enable reproducibility, and all methods share the same pretrained encoder to ensure that performance differences reflect the temporal modelling components rather than variations in spatial feature extraction.

### 5.1. Evaluation Protocol

All experiments employed 5-fold stratified cross-validation with strict subject-level partitioning to prevent data leakage between training and validation sets. The longitudinal dataset comprised 529 MRI scan pairs derived from 319 unique subjects, of which 84 were converters (patients who progressed from MCI to AD within the observation period) and 235 were non-converters (clinically stable MCI). Scan pairs were constructed from six visit combinations spanning intervals of 6 to 24 months: baseline to 6-month, baseline to 12-month, baseline to 24-month, 6-month to 12-month, 12-month to 24-month, and year-1 to year-2 follow-up visits.

Performance was assessed using three complementary metrics. The Area Under the Receiver Operating Characteristic Curve (AUC) served as the primary metric due to its threshold-independence and stability under class imbalance. Sensitivity (true positive rate) and F1-Score were employed as secondary metrics, reflecting the model’s ability to correctly identify converter patients and the harmonic balance between precision and recall, respectively.

## 5.2. Benchmark Methods

Three benchmark methods were evaluated, each utilising the identical pretrained encoder to ensure fair comparison of the temporal modelling components. The Siamese-Subtract architecture computes temporal change as the element-wise difference between encoded feature representations of paired scans, directly capturing the magnitude of structural change. The CNN-LSTM architecture processes the sequence of encoded features through a bidirectional LSTM layer to model temporal dependencies through recurrent connections. The TAFNet-InitialOnly configuration processes only the initial scan, bypassing the temporal fusion module entirely; this variant serves as a single-timepoint reference to isolate the contribution of longitudinal information.

## 5.3. Training Strategy

Training followed a two-phase transfer learning strategy designed to address the data scarcity inherent in longitudinal neuroimaging studies. In the first phase, the encoder was pretrained on 2,402 cross-sectional scans for cognitively normal versus AD classification, achieving a validation AUC of 0.922. In the second phase, the encoder weights were frozen, and only the Temporal Fusion Module and classification head ( $\sim 150\text{K}$  trainable parameters) were trained on longitudinal pairs. This strategy leverages the abundance of cross-sectional data to learn robust spatial feature representations while reserving the limited longitudinal pairs for learning temporal fusion.

# 6. Results and Analysis

This section presents a comprehensive evaluation of the proposed TAFNet architecture for predicting MCI-to-Alzheimer’s conversion from longitudinal structural MRI. The evaluation is organised into four components: comparative performance analysis against benchmark methods, ablation studies isolating the contributions of longitudinal information and scan interval and, interpretability analyses examining spatial attention and gate behaviour.

## 6.1. Comparative Performance

Table 1 presents the comparative performance of all evaluated methods. TAFNet achieved the highest AUC of  $0.916 \pm 0.044$ , representing improvements of 14.1% over Siamese-Subtract ( $0.803 \pm 0.055$ ), 1.9% over CNN-LSTM ( $0.899 \pm 0.055$ ), and 2.1% over the single-timepoint TAFNet-InitialOnly configuration ( $0.897 \pm 0.057$ ). Notably, TAFNet exhibited the lowest standard deviation among all methods, indicating more stable predictions across heterogeneous validation splits.

Table 1: Performance comparison for MCI-to-AD conversion prediction. Results report mean  $\pm$  standard deviation across 5-fold cross-validation on 529 longitudinal MRI pairs from 319 subjects. Bold indicates best performance per metric. Statistical significance assessed via Wilcoxon signed-rank test:  $*p < 0.05$  versus Siamese-Subtract.

Method	AUC	Sensitivity	F1-Score
Siamese-Subtract	$0.803 \pm 0.055$	$0.542 \pm 0.119$	$0.458 \pm 0.079$
CNN-LSTM	$0.899 \pm 0.055$	<b><math>0.646 \pm 0.114</math></b>	<b><math>0.601 \pm 0.138</math></b>
TAFNet-InitialOnly	$0.897 \pm 0.057$	$0.522 \pm 0.303$	$0.450 \pm 0.251$
<b>TAFNet (Proposed)</b>	<b><math>0.916 \pm 0.044^*</math></b>	$0.449 \pm 0.158$	$0.501 \pm 0.185$

The results reveal a notable divergence between discrimination and detection metrics. While TAFNet achieved the highest AUC, CNN-LSTM obtained superior Sensitivity (0.646) and F1-Score (0.601). This pattern reflects fundamentally different operating characteristics: TAFNet optimises for overall discrimination

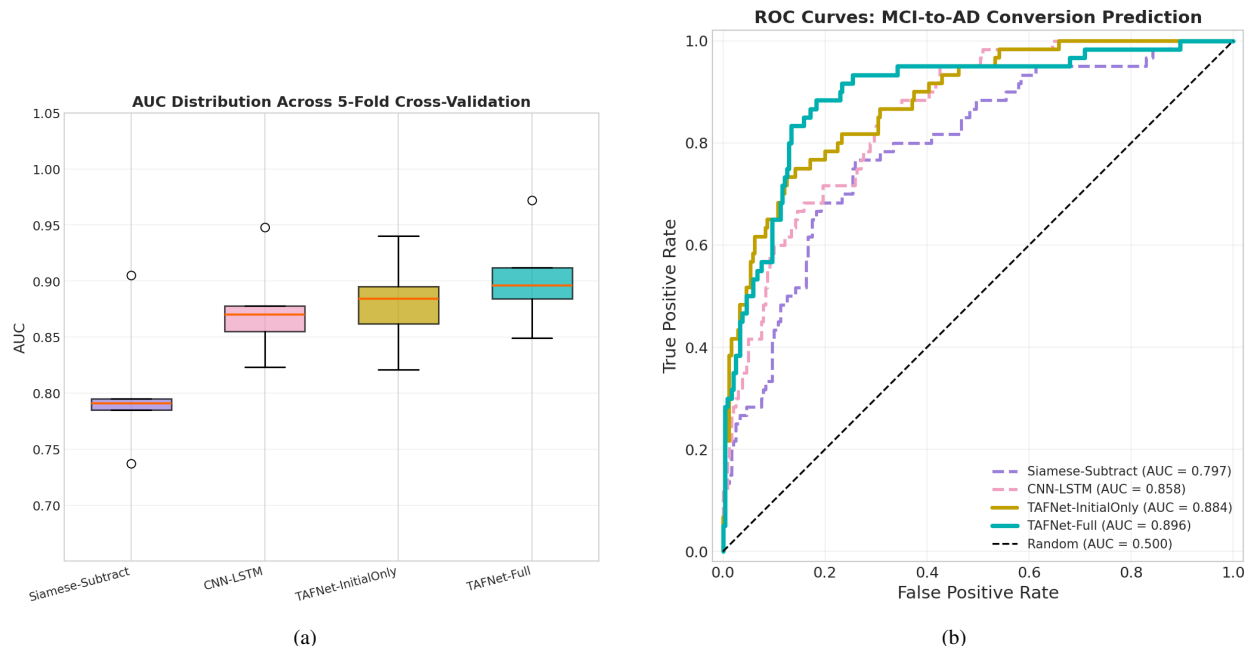


Figure 4: Performance comparison across benchmark methods and TAFNet variants. (a) Box plots showing AUC distribution across 5-fold cross-validation. TAFNet achieves the highest median AUC with competitive stability, while Siamese-Subtract exhibits greater variability with outliers at both extremes. (b) ROC curves computed from pooled predictions across all folds (pooled AUC values differ slightly from the fold-averaged means in Table 1). TAFNet dominates the upper-left region, indicating superior sensitivity-specificity trade-offs across all operating points.

with high specificity, whereas CNN-LSTM operates at a decision threshold that favours converter detection at the cost of increased false positives. The clinical implications of this trade-off are examined in Section 7.

To further characterise the discriminative performance of all methods, Fig. 4 presents two complementary visualisations. The box plot in Fig. 4(a) illustrates the distribution of AUC values across the five cross-validation folds. TAFNet exhibits not only the highest median AUC but also demonstrates competitive stability, with a compact interquartile range. Notably, the Siamese-Subtract method displays greater variability with outliers at both extremes of its distribution, indicating sensitivity to specific fold compositions that the attention-based methods mitigate through adaptive fusion. The attention-based architectures (CNN-LSTM, TAFNet-InitialOnly, and TAFNet) all demonstrate tighter distributions concentrated in the 0.82–0.95 range, with TAFNet achieving the highest upper quartile.

The receiver operating characteristic curves in Fig. 4(b) provide insight into discrimination capability across all classification thresholds. The ROC curves are computed from pooled predictions across all five folds, and therefore the associated AUC values differ slightly from the fold-averaged values reported in Table 1. TAFNet (pooled AUC = 0.896) consistently maintains the highest true positive rate for any given false positive rate, with its curve dominating the upper-left region of the ROC space. The progression from Siamese-Subtract (pooled AUC = 0.797) through CNN-LSTM (pooled AUC = 0.858) to TAFNet-InitialOnly (pooled AUC = 0.884) and finally TAFNet demonstrates the cumulative benefits of increasingly sophisticated temporal modelling. This characteristic is particularly valuable in clinical screening contexts where high sensitivity must be achieved while controlling specificity.

Fig. 5 illustrates the fold-wise AUC distribution for all four methods. TAFNet achieved the highest AUC in three of five folds, with particularly strong performance in Fold 1 (AUC = 0.973) and Fold 4 (AUC = 0.883). A consistent performance reduction was observed across all methods in Fold 2, which contained only 9 converter subjects in its validation partition. This uniform pattern confirms that the observed

variance reflects the challenging composition of that particular fold rather than any method-specific instability.

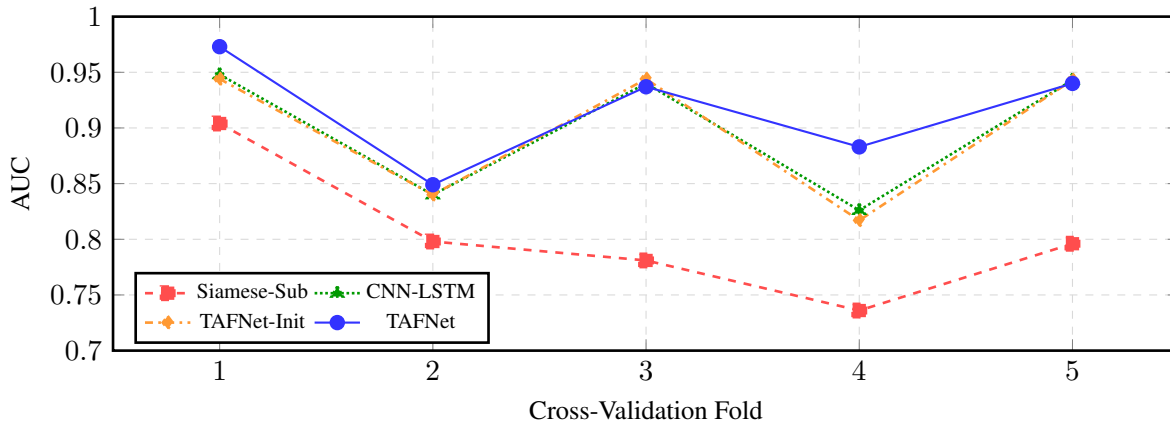


Figure 5: Fold-wise AUC performance across 5-fold cross-validation. TAFNet achieves the highest AUC in three of five folds. The consistent performance reduction in Fold 2 across all methods reflects the limited number of converter subjects ( $n = 9$ ) in that validation partition. Per-fold values: Siamese-Subtract (0.904, 0.798, 0.781, 0.736, 0.796); CNN-LSTM (0.948, 0.840, 0.940, 0.826, 0.943); TAFNet-InitialOnly (0.944, 0.840, 0.944, 0.817, 0.943); TAFNet (0.973, 0.849, 0.937, 0.883, 0.940).

Statistical significance was assessed using both pairwise and omnibus tests. For pairwise comparisons, the Wilcoxon signed-rank test was employed due to its appropriateness for small paired samples without distributional assumptions. As summarised in Table 2, TAFNet achieved statistically significant AUC improvement over Siamese-Subtract ( $p = 0.031$ ), prevailing in all five folds. The improvements over CNN-LSTM ( $\Delta = +0.017$ ) and TAFNet-InitialOnly ( $\Delta = +0.019$ ), while consistent in direction, did not reach significance at  $\alpha = 0.05$ . This outcome is expected given the modest effect sizes and the limited statistical power inherent to five-fold evaluation. For omnibus comparison, the Friedman test detected significant differences among all four methods ( $\chi^2 = 9.37$ ,  $p = 0.025$ ), confirming that method selection substantively impacts discriminative performance.

Table 2: Statistical significance of pairwise AUC comparisons. W/T/L denotes wins, ties, and losses across folds. Bold indicates significance at  $\alpha = 0.05$ .

Comparison	$\Delta$ AUC	W/T/L	$p$ -value
TAFNet vs Siamese-Subtract	+0.114	5/0/0	<b>0.031</b>
TAFNet vs CNN-LSTM	+0.017	3/0/2	0.156
TAFNet vs TAFNet-InitialOnly	+0.019	3/0/2	0.156
Friedman omnibus test: $\chi^2 = 9.37$ , $p = \mathbf{0.025}$			

To synthesise performance across all three metrics, average ranks were computed for each method within each fold and aggregated. TAFNet achieved the best mean rank for AUC (1.80), while CNN-LSTM achieved the best ranks for Sensitivity (2.10) and F1-Score (1.90). Across all metrics combined, TAFNet obtained the lowest overall mean rank (1.97), followed by CNN-LSTM (2.03), TAFNet-InitialOnly (2.30), and Siamese-Subtract (3.43). This ranking analysis confirms TAFNet as the most consistently competitive method when considering multiple evaluation criteria simultaneously.

## 6.2. Ablation Studies

To understand the sources of TAFNet’s performance gains, we conducted two controlled ablation studies. The first isolates the contribution of longitudinal temporal fusion by comparing TAFNet against

its single-timepoint variant. The second examines how scan interval duration and training set size jointly influence discriminative performance across all methods.

### 6.2.1. Contribution of Longitudinal Information

The controlled comparison between TAFNet and TAFNet-InitialOnly isolates the contribution of the temporal fusion module by holding all other architectural components constant. As presented in Table 3, incorporating the follow-up scan through the three-branch fusion mechanism yielded an AUC improvement from 0.897 to 0.916 (+2.1%) and an F1-Score improvement from 0.450 to 0.501 (+11.3%). The latter reflects enhanced precision-recall balance achieved through temporal fusion. Sensitivity exhibited a decrease from 0.522 to 0.449; however, this shift is accompanied by a substantial reduction in variance, as discussed below.

Table 3: Contribution of longitudinal information: TAFNet with temporal fusion versus initial scan only.

Configuration	AUC	Sensitivity	F1-Score
TAFNet-InitialOnly	0.897 ± 0.057	0.522 ± 0.303	0.450 ± 0.251
TAFNet (with fusion)	<b>0.916 ± 0.044</b>	0.449 ± 0.158	<b>0.501 ± 0.185</b>
Relative change	+2.1%	−14.0%	+11.3%

Beyond mean performance, the temporal fusion module conferred a marked improvement in prediction stability. The standard deviation of Sensitivity decreased from 0.303 to 0.158—a reduction of 48%—indicating substantially more consistent predictions across heterogeneous patient subgroups. This variance reduction carries clinical significance: it demonstrates that the Adaptive Temporal Gate successfully moderates the sensitivity to challenging validation partitions that characterises single-timepoint models. By dynamically weighting the three fusion branches (temporal difference, cross-attention, and concatenation) on a per-patient basis, the gate mechanism enables robust predictions even when any single fusion strategy would prove suboptimal.

Fig. 6 provides a visual summary of performance across all three metrics. The observed pattern reveals a fundamental trade-off in MCI conversion prediction: TAFNet maximises overall discrimination (highest AUC) with enhanced stability, whereas CNN-LSTM operates at a decision boundary that prioritises converter detection (highest Sensitivity and F1-Score). This trade-off reflects different clinical deployment scenarios. For population-level screening applications, where minimising false positives reduces unnecessary follow-up procedures and associated patient burden, TAFNet’s high-AUC operating point is preferable. For targeted monitoring of high-risk cohorts, where the cost of missing a converter outweighs that of false alarms, CNN-LSTM’s higher sensitivity may be more appropriate. The selection between these operating characteristics should ultimately be guided by the specific clinical context, institutional resources, and the relative costs assigned to false positive versus false negative predictions.

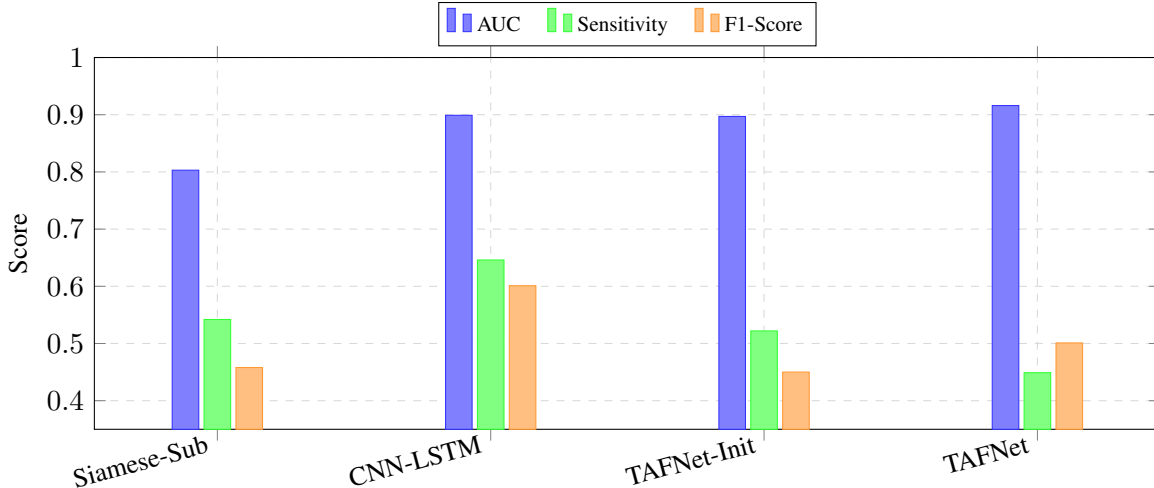


Figure 6: Performance comparison across AUC, Sensitivity, and F1-Score. TAFNet achieves the highest AUC, reflecting superior overall discrimination, while CNN-LSTM achieves the highest Sensitivity and F1-Score, reflecting a decision threshold optimised for converter detection.

### 6.2.2. Effect of Scan Interval and Data Efficiency

The pooled evaluation aggregates scan pairs across six visit combinations spanning 6–24 month intervals. To disentangle the contributions of scan interval duration and training set size, we conducted a stratified learning curve analysis. Table 4 reports AUC performance for each method when trained on 20%, 60%, and 100% of available pairs, stratified by the temporal gap between baseline and follow-up acquisitions. All configurations employed the identical frozen pretrained encoder to isolate the effects of temporal modelling.

Table 4: Learning curve analysis stratified by scan interval. AUC (mean  $\pm$  std) across 5-fold cross-validation. All methods use the frozen pretrained encoder. Best results per condition shown in **bold**.

Data Fraction	Method	6-month	12-month	24-month
20%	Siamese-Subtract	0.823 $\pm$ 0.136	0.829 $\pm$ 0.080	0.894 $\pm$ 0.027
	CNN-LSTM	0.905 $\pm$ 0.054	0.918 $\pm$ 0.026	0.933 $\pm$ 0.067
	TAFNet-InitialOnly	0.925 $\pm$ 0.050	0.928 $\pm$ 0.025	0.949 $\pm$ 0.059
	TAFNet	<b>0.933 <math>\pm</math> 0.056</b>	<b>0.932 <math>\pm</math> 0.024</b>	<b>0.949 <math>\pm</math> 0.059</b>
60%	Siamese-Subtract	0.749 $\pm$ 0.095	0.760 $\pm$ 0.077	0.784 $\pm$ 0.027
	CNN-LSTM	<b>0.905 <math>\pm</math> 0.052</b>	0.913 $\pm$ 0.026	<b>0.949 <math>\pm</math> 0.059</b>
	TAFNet-InitialOnly	0.901 $\pm$ 0.048	0.910 $\pm$ 0.023	<b>0.949 <math>\pm</math> 0.059</b>
	TAFNet	0.904 $\pm$ 0.053	<b>0.915 <math>\pm</math> 0.022</b>	<b>0.949 <math>\pm</math> 0.059</b>
100%	Siamese-Subtract	0.811 $\pm$ 0.065	0.778 $\pm$ 0.094	0.809 $\pm$ 0.054
	CNN-LSTM	0.909 $\pm$ 0.051	0.917 $\pm$ 0.026	0.949 $\pm$ 0.059
	TAFNet-InitialOnly	0.925 $\pm$ 0.044	0.928 $\pm$ 0.025	0.969 $\pm$ 0.059
	TAFNet	<b>0.928 <math>\pm</math> 0.057</b>	<b>0.933 <math>\pm</math> 0.027</b>	<b>0.969 <math>\pm</math> 0.059</b>

Three principal findings emerge from this analysis. First, longer scan intervals yield systematically higher discriminative performance across all methods. TAFNet achieved AUC of  $0.969 \pm 0.059$  on 24-month pairs compared to  $0.928 \pm 0.057$  on 6-month pairs when trained on all available data—a relative improvement of 4.4%. This gradient reflects the greater magnitude of detectable atrophy accumulated over longer

observation windows: the neurodegeneration signal captured in the temporal difference branch ( $\Delta f$ ) scales with interval duration, providing a stronger learning target for the fusion module. Importantly, this pattern persists even for the single-timepoint TAFNet-InitialOnly configuration, suggesting that patients scanned at longer intervals may exhibit more advanced baseline pathology that is itself predictive of conversion.

Second, TAFNet demonstrates exceptional data efficiency. With only 20% of training data, TAFNet achieved AUC exceeding 0.93 across all scan intervals, matching or exceeding the full-data performance of Siamese-Subtract. This finding has direct clinical implications: the adaptive fusion mechanism can deliver robust predictions even when longitudinal imaging data are scarce, a common constraint in prospective clinical cohorts where patient dropout and missed visits reduce available paired observations.

Third, the Siamese-Subtract baseline exhibits pronounced instability under data-limited conditions. At 20% data with 6-month intervals, Siamese-Subtract achieved AUC of  $0.823 \pm 0.136$ —a standard deviation nearly three times that of TAFNet ( $\pm 0.056$ ). More striking is the paradoxical performance degradation observed when increasing from 20% to 60% data: Siamese-Subtract AUC decreased from 0.823 to 0.749 at 6-month intervals. This counterintuitive pattern suggests that element-wise subtraction, while conceptually aligned with atrophy detection, lacks the representational capacity to generalise from heterogeneous training distributions. The Adaptive Temporal Gate mitigates this limitation by dynamically reweighting fusion strategies based on patient-specific feature characteristics, enabling consistent performance regardless of the specific training subset composition.

The convergence of TAFNet and TAFNet-InitialOnly at 24-month intervals (both achieving AUC = 0.969) warrants interpretation. At this extended temporal horizon, baseline structural vulnerability may dominate the predictive signal, reducing the marginal contribution of explicit temporal fusion. Nevertheless, TAFNet maintains an advantage at shorter intervals where the atrophy signal is subtler, confirming that the three-branch fusion mechanism extracts complementary information that single-timepoint models cannot access.

Collectively, these results validate the multi-interval pooling strategy employed in the main evaluation: by combining scan pairs across 6–24 month intervals, the training procedure exposes the fusion module to diverse temporal dynamics, enabling robust generalisation across the heterogeneous progression trajectories characteristic of MCI cohorts. The stratified analysis further demonstrates that TAFNet’s architectural advantages—adaptive gating, cross-temporal attention, and residual baseline preservation—translate to consistent discriminative gains across clinically relevant variations in scan timing and data availability.

### 6.3. Interpretability Analysis

A key requirement for clinical adoption of deep learning models is the ability to provide interpretable explanations for predictions. This subsection examines two complementary interpretability mechanisms intrinsic to TAFNet: spatial attention maps that reveal which brain regions drive predictions, and adaptive gate coefficients that quantify the relative contribution of each temporal fusion strategy.

#### 6.3.1. Spatial Attention Maps

To understand which brain regions drive TAFNet’s predictions, we extracted spatial attention maps from the encoder’s bottleneck layer and visualised them as heatmap overlays on the anatomical MRI. Figure 7 presents attention distributions for a representative MCI subject, while Figure 8 shows the average attention pattern across ten subjects in the evaluation cohort.

The attention maps reveal consistent focus on structures known to be affected early in Alzheimer’s disease progression. In the sagittal view, pronounced activation appears along the corpus callosum, cingulate gyrus, and medial temporal regions including the hippocampal formation. The coronal sections demonstrate bilateral attention to the lateral ventricles and surrounding periventricular white matter, with additional focus on the temporal horns and hippocampi. Axial slices show a characteristic pattern of high activation in central

brain structures, particularly around the ventricular system and deep gray matter nuclei, with progressively lower attention toward the cortical periphery.

The spatial distribution of attention aligns with established neuroanatomical knowledge of AD pathology. Ventricular enlargement serves as a macroscopic marker of generalised brain atrophy, and the model’s sensitivity to periventricular boundaries suggests it has learned to detect the structural signatures of neurodegeneration. The concentration of attention in medial temporal structures is consistent with the Braak staging of neurofibrillary tangle accumulation, which begins in the transentorhinal and entorhinal cortex before spreading to the hippocampus and eventually to widespread neocortical regions. The model appears to have discovered these clinically meaningful biomarkers without explicit anatomical supervision, relying solely on the conversion labels during training.

Figure 9 presents a multi-slice axial view spanning inferior to superior brain levels. The attention pattern varies systematically across the brain: inferior slices show high activation in the temporal poles and cerebellum, mid-brain slices exhibit the strongest attention around the lateral ventricles and basal ganglia, and superior slices demonstrate more diffuse cortical activation with residual focus on the longitudinal fissure. This gradient reflects the known topography of AD-related atrophy, which is most pronounced in limbic and paralimbic structures and relatively preserved in primary sensory and motor cortices until later disease stages.

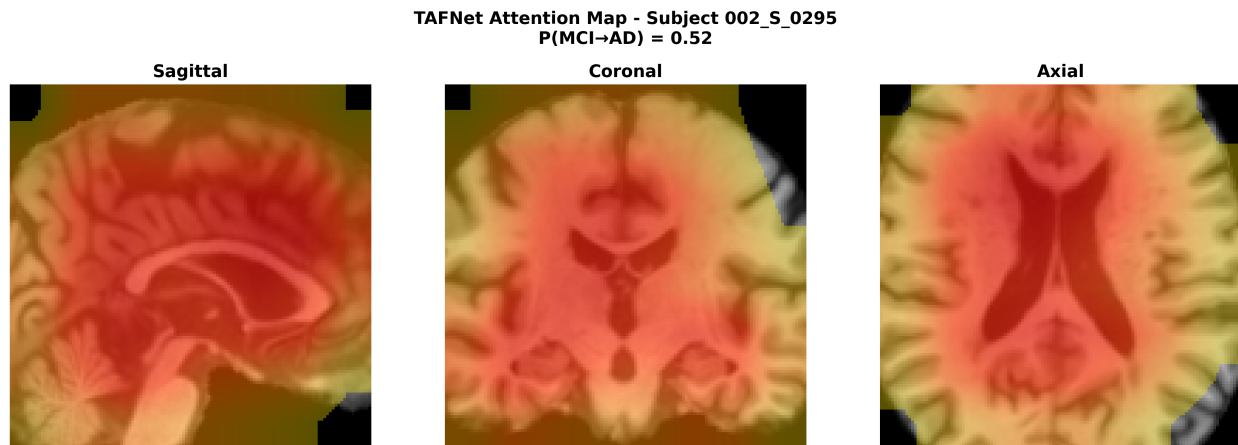


Figure 7: Attention heatmap for a representative MCI subject (002\_S\_0295) with predicted conversion probability  $P(\text{MCI} \rightarrow \text{AD}) = 0.52$ . Warmer colours indicate regions receiving greater model attention. Notable concentrations appear in periventricular regions, medial temporal lobes, and the corpus callosum.

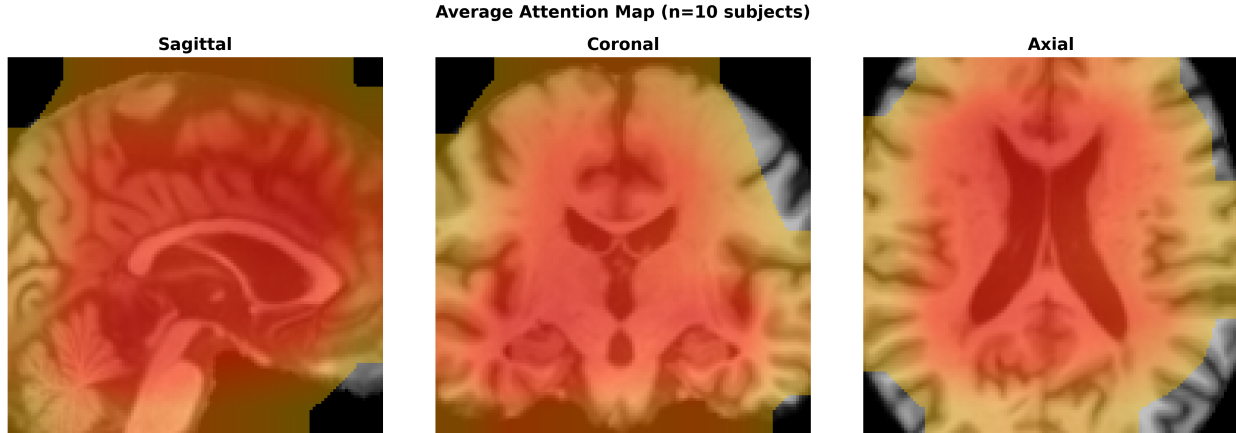


Figure 8: Average attention map computed across  $n = 10$  subjects in the evaluation cohort. The consistent pattern across subjects demonstrates that TAFNet has learned generalisable anatomical features rather than subject-specific artefacts.

The consistency of attention patterns across subjects, as evidenced by the aggregate map in Figure 8, suggests that TAFNet has learned generalisable features of disease progression rather than overfitting to subject-specific characteristics. This consistency is particularly notable given the heterogeneity of MCI populations, which include individuals with varying rates of cognitive decline and different underlying pathologies. The interpretability afforded by these visualisations addresses a critical concern in the clinical deployment of deep learning models, providing clinicians with anatomically grounded explanations for the model’s predictions.

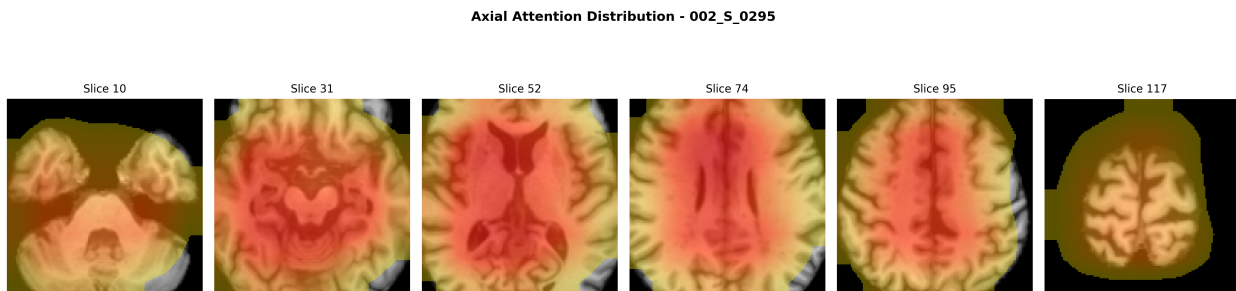


Figure 9: Axial attention distribution across six representative slices from inferior (left) to superior (right). The attention pattern varies systematically, with strongest activation in mid-brain structures surrounding the lateral ventricles.

### 6.3.2. Adaptive Gate Coefficient Analysis

The Temporal Fusion Module employs three parallel branches whose contributions are dynamically weighted by learned gate coefficients:  $\alpha$  for the temporal subtraction branch,  $\beta$  for the cross-attention branch, and  $\gamma$  for the concatenation branch. These coefficients are computed via a softmax-normalised gating network and sum to unity for each subject, allowing the model to adaptively emphasise different fusion strategies based on individual scan characteristics.

Table 5 summarises the gate coefficient statistics across the evaluation cohort of 33 subjects. The temporal subtraction branch received the highest mean weight ( $\alpha = 0.437 \pm 0.013$ ), significantly exceeding the uniform baseline of 0.333 ( $p < 10^{-29}$ ). The cross-attention branch received a substantially lower weight ( $\beta = 0.254 \pm 0.009$ ), significantly below the uniform baseline ( $p < 10^{-30}$ ). The concatenation branch received an intermediate weight ( $\gamma = 0.309 \pm 0.004$ ), also significantly below uniform ( $p < 10^{-25}$ ). Notably, the temporal subtraction branch was dominant (highest weight) for all 33 subjects, with no subjects favouring

Table 5: Adaptive gate coefficient statistics across the evaluation cohort ( $n = 33$ ). The temporal subtraction branch ( $\alpha$ ) receives consistently higher weight than the cross-attention ( $\beta$ ) and concatenation ( $\gamma$ ) branches. All coefficients differ significantly from the uniform baseline of 0.333.

Coefficient	Branch	Mean	Std	Min	Max	$p$ -value
$\alpha$	Temporal Subtraction	0.437	0.013	0.408	0.457	$< 10^{-29}$
$\beta$	Cross-Attention	0.254	0.009	0.240	0.277	$< 10^{-30}$
$\gamma$	Concatenation	0.309	0.004	0.301	0.316	$< 10^{-25}$

either the cross-attention or concatenation branches.

Figure 10 visualises the distribution of gate coefficients across subjects. The boxplot demonstrates that  $\alpha$  consistently exceeds the equal-weighting threshold (dashed line at 0.333), while  $\beta$  falls substantially below this threshold and  $\gamma$  clusters just below it. The remarkably low variance across all three coefficients ( $\sigma_\alpha = 0.013$ ,  $\sigma_\beta = 0.009$ ,  $\sigma_\gamma = 0.004$ ) indicates that the adaptive gating mechanism has converged to a highly stable operating point for this task.

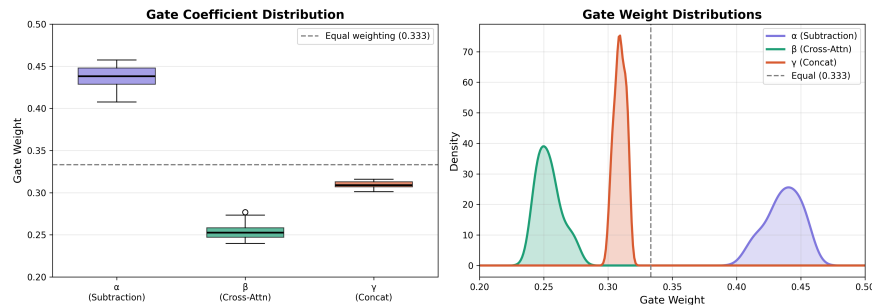


Figure 10: Distribution of adaptive gate coefficients across the evaluation cohort ( $n = 33$ ). The temporal subtraction branch ( $\alpha$ ) consistently receives the highest weight, exceeding the equal-weighting baseline (dashed line at 0.333). The cross-attention branch ( $\beta$ ) receives the lowest weight. The low variance across all coefficients indicates a stable fusion strategy.

The dominance of the temporal subtraction branch has important implications for understanding the model’s decision-making process. Temporal subtraction explicitly captures volumetric changes between baseline and follow-up scans, suggesting that the rate of structural change is a more informative predictor of conversion than either the cross-temporal attention relationships captured by  $\beta$  or the bilateral feature preservation captured by  $\gamma$ . This finding is consistent with clinical evidence that the trajectory of decline, rather than a single snapshot, provides the most prognostic value for predicting MCI-to-AD conversion. The model has effectively learned to prioritise longitudinal change detection, which aligns with the fundamental motivation for acquiring paired scans in clinical practice.

Figure 11 presents the relationship between gate coefficients and model predictions. Strikingly,  $\alpha$  exhibits a strong positive correlation with conversion probability ( $r = 0.825$ ,  $p < 10^{-8}$ ), indicating that subjects with higher predicted risk receive greater weight on the temporal subtraction branch. Conversely,  $\beta$  shows a strong negative correlation ( $r = -0.835$ ,  $p < 10^{-9}$ ), and  $\gamma$  shows a moderate negative correlation ( $r = -0.720$ ,  $p < 10^{-5}$ ). These relationships suggest that the gating mechanism has learned to amplify the contribution of explicit change detection for subjects exhibiting more pronounced neurodegeneration, while reducing reliance on cross-attention features. The tight clustering of predictions around  $P(\text{MCI} \rightarrow \text{AD}) \approx 0.52$  reflects the near-threshold nature of many MCI cases in this cohort.

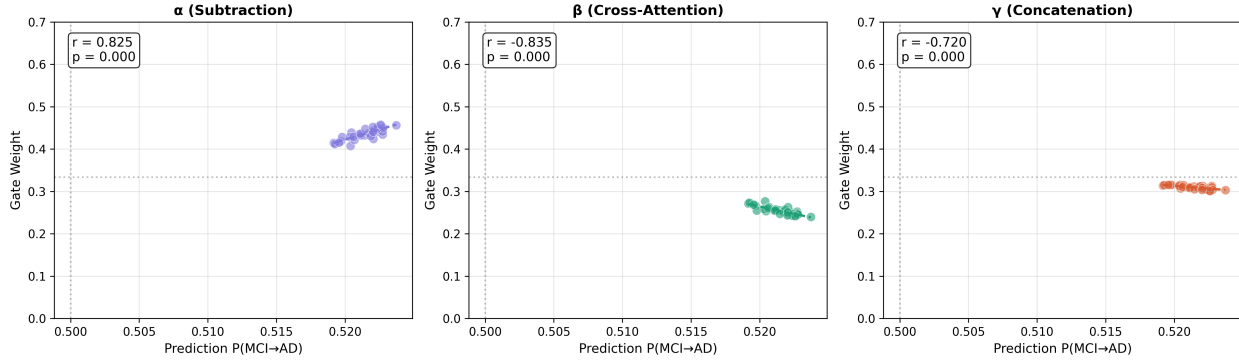


Figure 11: Relationship between gate coefficients and conversion predictions. The temporal subtraction coefficient ( $\alpha$ ) shows a strong positive correlation with predicted conversion probability ( $r = 0.825$ ), while cross-attention ( $\beta$ ,  $r = -0.835$ ) and concatenation ( $\gamma$ ,  $r = -0.720$ ) show negative correlations. Dashed lines indicate the decision threshold (vertical) and equal-weighting baseline (horizontal).

The stability of gate weights across subjects, combined with the strong correlation between  $\alpha$  and prediction confidence, provides evidence that the adaptive gating mechanism serves a meaningful role in the model’s decision-making process. Rather than producing arbitrary or inconsistent weightings, the gate network has learned a systematic strategy: subjects with more detectable structural change receive predictions driven predominantly by the temporal subtraction branch, while the cross-attention and concatenation branches provide complementary information that modulates the final output. This interpretable behaviour supports the clinical validity of TAFNet’s predictions and suggests that the three-branch architecture captures genuinely distinct aspects of longitudinal disease progression.

The experimental evaluation establishes that TAFNet achieves state-of-the-art discriminative performance for MCI-to-AD conversion prediction. The proposed architecture attained the highest AUC (0.916) among all evaluated methods, with statistically significant improvement over the Siamese-Subtract baseline ( $p = 0.031$ ) and the lowest cross-fold variance ( $SD = 0.044$ ). The controlled comparison with TAFNet-InitialOnly confirmed that incorporating longitudinal information through temporal fusion improves both AUC (+2.1%) and F1-Score (+11.3%), while reducing prediction variance by 48%. Although CNN-LSTM achieved higher Sensitivity and F1-Score at its default operating point, TAFNet’s superior AUC indicates better overall patient ranking by conversion risk—the clinically relevant criterion for prioritising limited follow-up resources. The stratified analysis demonstrated exceptional data efficiency, with TAFNet matching or exceeding baseline full-data performance using only 20% of training pairs, and revealed that longer scan intervals yield systematically higher discrimination across all methods. Interpretability analyses provided converging evidence of biological plausibility: spatial attention maps focused on medial temporal and periventricular structures consistent with established AD pathology, while the consistent dominance of the temporal subtraction gate ( $\alpha = 0.437$ ) and its strong correlation with conversion probability ( $r = 0.825$ ) confirmed that the adaptive mechanism captures clinically meaningful variation in disease presentation. These findings validate both the architectural design of the three-branch adaptive fusion mechanism and the clinical value of incorporating disease progression trajectories into predictive models for Alzheimer’s disease.

## 7. Discussion

The experimental results demonstrate that TAFNet achieves competitive discriminative performance for MCI-to-AD conversion prediction using only longitudinal structural MRI. This section first contextualises these findings against the broader published literature to establish where TAFNet stands relative to alternative approaches and modalities. It then examines the clinical implications of the observed performance character-

istics, analyses the biological plausibility of learned representations, acknowledges limitations, and identifies directions for future research.

### 7.1. Comparison with Published Literature

To contextualise TAFNet’s performance beyond the internal baselines reported in Section 6.1, Table 6 compares our results against published methods for MCI-to-AD conversion prediction on the ADNI cohort. We organise the comparison by input modality, distinguishing MRI-only approaches from multimodal methods that additionally incorporate clinical assessments, cerebrospinal fluid biomarkers, positron emission tomography, or genetic information. Direct numerical comparison across studies requires caution due to differences in cohort composition, conversion time horizons, cross-validation schemes, and class imbalance handling; nonetheless, the reported AUC values provide a useful reference frame.

Table 6: Comparison with published methods for MCI-to-AD conversion prediction on the ADNI cohort. Methods are grouped by input modality. Horizon denotes the conversion observation window.  $N_{\text{MCI}}$  indicates the number of MCI subjects used. Direct comparison across studies requires caution due to differences in cohort selection, validation strategy, and class balance.

Study	Method	Modality	Horizon	$N_{\text{MCI}}$	AUC	Validation
<i>Structural MRI only</i>						
Bron et al. [40]	SVM / CNN	sMRI	3 yr	859	0.62–0.82	External
Lin et al. [41]	3D CNN	sMRI	3 yr	345	0.861	10-fold CV
Aghajanian et al. [18]	CNN + LSTM	Long. sMRI	var.	228	0.80–0.90 <sup>†</sup>	5-fold CV
<b>TAFNet (ours)</b>	<b>CNN-Transformer</b>	<b>Long. sMRI</b>	<b>3 yr</b>	<b>319</b>	<b>0.916</b>	<b>5-fold CV</b>
<i>Multimodal (MRI + clinical / CSF / PET / genetic)</i>						
Spasov et al. [42]	Multi-stream CNN	sMRI + clin. + APOE	3 yr	785	0.925	10-fold CV
Liu et al. [43]	ELM grading	sMRI + PET + CSF + APOE	3 yr	476	0.888	10-fold CV
Lee et al. [44]	Multimodal RNN	sMRI + CSF + cog.	2 yr	347	0.93	5-fold CV
Chen et al. [45]	Meta-analysis (18 studies)	Various	var.	var.	0.67–0.98	Various
Wang et al. [46]	DISFC	sMRI + clin. + genetic	4 yr	252	0.962	10-fold CV

<sup>†</sup>Reported as concordance index (c-index) rather than AUC; approximate equivalence assumed.

Among MRI-only approaches, TAFNet’s AUC of 0.916 substantially exceeds the 0.62–0.82 range reported by Bron et al. [40] in a rigorous cross-cohort evaluation spanning multiple ADNI waves, and surpasses the 0.861 achieved by Lin et al. [41] using a 3D CNN on baseline scans. Compared to the recent longitudinal MRI work of Aghajanian et al. [18], which combined CNN embeddings with time-aware LSTMs and reported concordance indices of 0.80–0.90, TAFNet demonstrates that adaptive multi-branch fusion can extract additional prognostic information from longitudinal pairs beyond what sequential recurrent processing captures.

Perhaps more striking is the comparison with multimodal methods. TAFNet’s MRI-only AUC of 0.916 approaches the 0.925 reported by Spasov et al. [42], who additionally incorporated clinical assessments and APOE genotype, and exceeds the 0.888 achieved by Liu et al. [43] with four input modalities (MRI, FDG-PET, CSF, and APOE). Only methods that combine MRI with extensive clinical and genetic features—such as the DISFC model of Wang et al. [46] (AUC = 0.962) or the longitudinal multimodal LSTM of Lee et al. [44] (AUC = 0.93)—clearly surpass TAFNet’s performance. However, these multimodal approaches require data sources that are substantially more expensive, invasive, or clinically restricted than structural MRI. PET imaging involves radiopharmaceutical exposure, CSF collection requires lumbar puncture, and genetic testing introduces additional regulatory and consent requirements. The meta-analysis of Chen et al. [45] reinforces this pattern, reporting development AUC values spanning 0.67–0.98 across 18 studies, with MRI, APOE $\epsilon$ 4, MMSE, and ADAS-cog emerging as the most prevalent and strongest predictors.

These comparisons support the interpretation that TAFNet achieves near-multimodal predictive performance from a single, widely accessible, non-invasive imaging modality. Structural MRI is routinely

acquired in clinical practice, requires no radioactive tracers or invasive fluid collection, and is available across virtually all healthcare settings. The clinical value proposition is therefore not that TAFNet necessarily exceeds multimodal approaches, but that it substantially narrows the performance gap while relying exclusively on data that is already routinely collected. For healthcare systems lacking access to PET, CSF analysis, or comprehensive genetic testing, TAFNet offers a practical and competitive alternative.

Furthermore, the architecture is not inherently limited to MRI; future integration of complementary biomarkers through additional fusion branches represents a natural extension that may close the remaining performance gap with the best multimodal methods. Indeed, recent work has demonstrated that deep survival models operating on baseline CSF biomarkers alone can achieve a concordance index of 0.83 for MCI-to-dementia conversion with calibrated uncertainty quantification [47], suggesting that combining imaging-derived temporal features with fluid biomarker prognostication represents a particularly promising fusion strategy.

### 7.2. *Clinical Deployment Considerations*

The divergence between TAF-Net and CNN-LSTM across evaluation metrics reflects fundamentally different clinical operating points. TAF-Net achieved the highest AUC (0.916) and specificity (0.939) but lower sensitivity (0.449), while CNN-LSTM achieved superior sensitivity (0.646) and F1-score (0.601) at the cost of reduced specificity (0.842). This trade-off has direct implications for clinical deployment scenarios. For population-level screening applications, where the cost of false positives includes unnecessary diagnostic procedures, patient anxiety, and healthcare resource expenditure, TAF-Net’s high-specificity operating point is preferable. In contrast, for targeted monitoring of individuals already identified as high-risk, such as APOE  $\epsilon$ 4 carriers with biomarker evidence of amyloid pathology, CNN-LSTM’s higher sensitivity may be more appropriate, as the cost of missing a converter outweighs that of additional monitoring.

For clinical trial enrichment, where maximizing converter enrollment is paramount, the sensitivity-optimized operating point of CNN-LSTM would facilitate efficient patient recruitment. More broadly, TAFNet’s risk scores could serve as inputs to systematic trial design optimisation frameworks; recent work has demonstrated that multi-objective optimisation can identify Pareto-optimal eligibility configurations that balance recruitment feasibility, cost efficiency, and patient identification accuracy for AD trials [48], and integrating imaging-derived conversion risk estimates into such frameworks represents a natural extension for enriching trial populations with likely converters.

Importantly, TAF-Net’s superior AUC indicates better overall patient ranking by conversion risk, which represents the clinically relevant criterion for prioritizing limited follow-up resources. A model with higher AUC allows clinicians to select an operating threshold that balances sensitivity and specificity according to institutional resources and patient preferences, whereas a lower AUC model constrains the achievable trade-offs regardless of threshold selection.

The 48% reduction in sensitivity variance achieved by TAF-Net compared to TAF-Net-InitialOnly carries additional clinical significance. High variance in model predictions across patient subgroups undermines clinical trust and complicates deployment in diverse populations. The Adaptive Temporal Gate’s ability to moderate sensitivity to challenging patient presentations suggests more robust real-world performance than single-timepoint alternatives.

### 7.3. *Biological Plausibility of Learned Representations*

The interpretability analyses provide evidence that TAF-Net has learned biologically plausible representations of AD-related neurodegeneration, despite receiving no explicit anatomical supervision during training. The spatial attention maps demonstrate pronounced focus on the medial temporal lobe, including the hippocampus and entorhinal cortex, and the periventricular white matter. This pattern aligns with the Braak staging system for neurofibrillary tangle accumulation [49], which identifies these structures as the earliest sites of tau pathology in AD. The attention gradient, strongest in medial temporal structures, moderate in

the cingulate and precuneus, and weaker in lateral neocortex, mirrors the known topography of AD-related atrophy [9]. The model’s sensitivity to ventricular boundaries is particularly notable. Ventricular enlargement has been extensively validated as an objective and sensitive progression marker in ADNI [13], and longitudinal ventricular expansion rates predict conversion from MCI to AD [12]. TAF-Net appears to have independently discovered this clinically established biomarker through end-to-end learning from conversion labels alone.

The consistent dominance of the temporal subtraction branch ( $\alpha = 0.437$ , highest for all 33 subjects) indicates that the model prioritizes explicit volumetric change over static features or cross-temporal correlations. This finding aligns with clinical evidence that rates of brain shrinkage provide prognostic information beyond what single scans can capture [12, 14]. The strong positive correlation between  $\alpha$  and conversion probability ( $r = 0.825$ ) further supports biological plausibility: subjects exhibiting more pronounced structural change receive predictions driven predominantly by the change-detection branch, mirroring clinical reasoning where physicians weigh observed atrophy rate more heavily in patients showing rapid decline.

#### 7.4. Limitations

Several limitations of this study warrant acknowledgment and inform directions for future research. All experiments were conducted on the ADNI cohort, a carefully curated research dataset with standardized imaging protocols across sites. While ADNI represents the gold standard for AD neuroimaging research, it may not reflect the heterogeneity of real-world clinical populations. Acquisition parameters, patient demographics, and diagnostic criteria vary substantially across healthcare systems, and external validation on independent clinical cohorts such as the National Alzheimer’s Coordinating Center database or institutional datasets is essential before clinical deployment. The dataset exhibits substantial class imbalance, with only 84 converters (26.3%) among 319 subjects. While we employed class-weighted loss and stratified cross-validation to mitigate this imbalance, the limited number of positive examples constrains model learning and statistical power. The sensitivity variance observed across folds partially reflects this constraint.

TAF-Net requires paired scans with a minimum interval of approximately 6 months to capture detectable structural change. This requirement limits applicability in acute clinical decision-making scenarios where immediate risk stratification is needed. For patients presenting without prior imaging history, the single-timepoint TAF-Net-InitialOnly configuration provides a reasonable alternative with AUC of 0.897, though with reduced discriminative power. The gate coefficient analysis was conducted on 33 subjects with conversion probabilities clustered around 0.52. This narrow prediction range limits interpretation of gate behavior across the full risk spectrum, and the absence of clearly low-risk subjects prevents assessment of whether gate behavior differs meaningfully between high-risk and low-risk populations. This study focused exclusively on T1-weighted structural MRI, excluding other established AD biomarkers including amyloid-PET, tau-PET, cerebrospinal fluid markers, and emerging blood-based biomarkers. While structural MRI offers advantages of accessibility and non-invasiveness, multimodal integration may yield superior predictive performance, particularly for early-stage cases where structural changes are subtle.

#### 7.5. Future Directions

The findings of this study suggest several promising directions for future research, spanning external validation, architectural extensions, and clinical translation.

##### 7.5.1. External Validation and Multimodal Integration

Priority should be given to external validation on geographically and demographically diverse cohorts. The National Alzheimer’s Coordinating Center database, comprising data from over 30 Alzheimer’s Disease Research Centers, provides an ideal validation target for assessing generalisation across different scanner manufacturers, acquisition protocols, and clinical populations. Extending TAFNet to incorporate complementary biomarkers, particularly amyloid-PET for pathological confirmation and blood-based markers such

as plasma p-tau217 and GFAP for accessibility, may improve both discriminative performance and clinical utility. The Temporal Fusion Module’s architecture could be adapted to process multimodal longitudinal data, with separate branches for imaging and fluid biomarker trajectories. A dual-model framework for CSF-based prognostication has recently demonstrated that baseline fluid biomarkers can provide both survival prediction and calibrated cognitive decline trajectories from a single assessment [47], establishing a natural complement to TAFNet’s imaging-derived temporal features.

### 7.5.2. Time-to-Event Prediction and MCI Subtype Stratification

The current binary classification formulation discards information about time-to-conversion. Reformulating the task as time-to-event prediction using survival analysis frameworks would provide clinically actionable conversion risk timelines rather than dichotomous classifications, enabling clinicians to tailor monitoring schedules and intervention timing to individual risk profiles.

A particularly compelling clinical application lies in differentiating MCI trajectories. MCI is a heterogeneous condition: while a substantial proportion of patients progress to AD, many remain stable for years, and some revert to normal cognition [7, 6]. Understanding what distinguishes these subpopulations is essential for clinical decision-making, yet current models, including TAFNet, treat all MCI patients as a homogeneous group. Future work could leverage TAFNet’s learned representations to characterise distinct trajectory subtypes. For instance, the gate coefficients ( $\alpha, \beta, \gamma$ ) and spatial attention patterns may differ systematically between patients who convert rapidly, those who convert slowly, and those who remain stable, providing imaging-derived signatures of trajectory subtype. Identifying such signatures would enable a more nuanced clinical decision support tool: rather than a single binary prediction, clinicians could be presented with a patient’s predicted trajectory alongside the structural brain features driving that prediction. For patients identified as rapid converters, this could motivate earlier pharmacological intervention with emerging disease-modifying therapies, intensified cognitive monitoring, or prioritisation for clinical trial enrolment. For patients predicted to remain stable, it could reduce unnecessary invasive testing and associated patient anxiety.

A complementary approach to trajectory differentiation is counterfactual explanation, which identifies the smallest changes to input features that would alter a model’s prediction to a desired outcome [50]. Applied to TAFNet, counterfactual analysis could reveal which specific structural changes—or absence thereof—would shift a patient’s predicted trajectory from converter to stable, effectively generating personalised “what-if” scenarios. For instance, a counterfactual might indicate that a modest reduction in ventricular expansion rate or preservation of hippocampal volume above a certain threshold would be sufficient to shift the prediction, providing clinicians with interpretable, actionable targets for monitoring. Multi-objective formulations of counterfactual search are particularly well suited to this setting, as they can simultaneously optimise for proximity to the original patient, sparsity of feature changes, and plausibility with respect to the observed population, returning a diverse set of clinically meaningful alternatives rather than a single explanation [50]. Integrating such counterfactual reasoning with TAFNet’s gate coefficients and spatial attention maps could yield a rich clinical decision support tool that not only predicts trajectory but also explains what distinguishes different predicted outcomes at the individual patient level.

### 7.5.3. Network-Based Disease Trajectory Analysis

An emerging methodological direction is the application of network analysis to model the evolving landscape of comorbidities preceding AD diagnosis. Recent work in multiple sclerosis has demonstrated that disease co-occurrence networks constructed from longitudinal health records can reveal prodromal reorganisation patterns, including rewired diagnostic hubs and multisystem clustering, that are not detectable through static comorbidity counts alone [51]. This approach characterises how the structural position of individual diagnoses within a patient’s comorbidity network changes over time, providing a systems-level view of disease emergence.

Applying such network-based trajectory analysis to MCI and AD populations represents a natural extension of the present work. The ADNI dataset includes longitudinal clinical, cognitive, and biomarker data that could be modelled as evolving diagnostic networks, enabling investigation of whether MCI patients who ultimately convert to AD exhibit distinct network signatures, such as increasing connectivity among neuropsychiatric, metabolic, and inflammatory diagnoses, in the years preceding conversion. Integrating imaging-derived risk scores from TAFNet with network-based comorbidity trajectories could yield a multi-modal clinical decision support framework that captures both the structural brain changes visible on MRI and the broader systemic context of disease progression.

#### 7.5.4. Extension to Other Neurodegenerative Conditions

The TAFNet architecture is not specific to Alzheimer’s disease, and similar longitudinal fusion approaches may benefit prediction tasks in other neurodegenerative conditions characterised by progressive structural change, including frontotemporal dementia, Parkinson’s disease dementia, and multiple sclerosis progression.

## 8. Conclusion

This paper introduced TAF-Net, a hybrid CNN-Transformer architecture for predicting 3-year MCI-to-AD conversion from paired longitudinal structural MRI. The core contribution is the Temporal Fusion Module, which integrates three complementary fusion strategies—temporal subtraction, cross-temporal attention, and feature concatenation—governed by an Adaptive Temporal Gate that learns patient-specific weighting. Extensive evaluation on the ADNI cohort demonstrated that TAF-Net achieves state-of-the-art discriminative performance with AUC of  $0.916 \pm 0.044$ , representing statistically significant improvement over the Siamese-Subtract baseline ( $p = 0.031$ ) and exhibiting the lowest cross-fold variance among all evaluated methods. Ablation studies confirmed that incorporating longitudinal information through temporal fusion improves both discrimination (+2.1% AUC) and prediction stability (48% variance reduction), while analysis of scan intervals revealed that longer observation windows yield systematically higher performance across all methods. Interpretability analyses provided evidence of biological plausibility: spatial attention maps focused on medial temporal and periventricular structures consistent with established AD pathology, while the dominance of the temporal subtraction branch ( $\alpha = 0.437$ ) aligned with clinical emphasis on atrophy rate over static volumetric measures. The strong correlation between gate coefficients and conversion probability ( $r = 0.825$ ) demonstrates that the adaptive mechanism captures clinically meaningful variation in disease presentation. These findings validate the hypothesis that intelligently integrating temporal trajectories through adaptive fusion yields a decidedly superior and more reliable prognostic tool for neurodegenerative disease modeling. Future work will focus on external validation across diverse clinical cohorts, multimodal integration with complementary biomarkers, and extension to related neurodegenerative conditions.

## Acknowledgements

Data collection and sharing for the Alzheimer’s Disease Neuroimaging Initiative (ADNI) is funded by the National Institute on Aging (National Institutes of Health Grant U19AG024904). The grantee organization is the Northern California Institute for Research and Education. In the past, ADNI has also received funding from the National Institute of Biomedical Imaging and Bioengineering, the Canadian Institutes of Health Research, and private sector contributions through the Foundation for the National Institutes of Health (FNIH) including generous contributions from the following: AbbVie, Alzheimer’s Association; Alzheimer’s Drug Discovery Foundation; Araclon Biotech; BioClinica, Inc.; Biogen; Bristol-Myers Squibb Company; CereSpir, Inc.; Cogstate; Eisai Inc.; Elan Pharmaceuticals, Inc.; Eli Lilly and Company; EuroImmun; F. Hoffmann-La Roche Ltd and its affiliated company Genentech, Inc.; Fujirebio; GE Healthcare; IXICO Ltd.; Janssen

Alzheimer Immunotherapy Research & Development, LLC.; Johnson & Johnson Pharmaceutical Research & Development LLC.; Lumosity; Lundbeck; Merck & Co., Inc.; Meso Scale Diagnostics, LLC.; NeuroRx Research; Neurotrack Technologies; Novartis Pharmaceuticals Corporation; Pfizer Inc.; Piramal Imaging; Servier; Takeda Pharmaceutical Company; and Transition Therapeutics.

### Author Contributions

**Alireza Moayedikia:** Conceptualization, Methodology, Software, Formal analysis, Investigation, Data curation, Writing – original draft, Writing – review & editing, Visualization, Project administration. **Sara Fin:** Conceptualization, Methodology, Validation, Writing – review & editing, Supervision. **Alicia Troncoso:** Writing – review & editing, Supervision. **Uffe Kock Wiil:** Writing – review & editing, Supervision.

### References

- [1] Philip Scheltens, Bart De Strooper, Miia Kivipelto, Henne Holstege, Gaël Chételat, Charlotte E. Teunissen, Jeffrey Cummings, and Wiesje M. van der Flier. Alzheimer's disease. *The Lancet*, 397 (10284):1577–1590, 2021. doi: 10.1016/S0140-6736(20)32205-4.
- [2] Clifford R. Jack, David S. Knopman, William J. Jagust, Leslie M. Shaw, Paul S. Aisen, Michael W. Weiner, Ronald C. Petersen, and John Q. Trojanowski. Hypothetical model of dynamic biomarkers of the Alzheimer's pathological cascade. *The Lancet Neurology*, 9(1):119–128, 2010. doi: 10.1016/S1474-4422(09)70299-6.
- [3] Clifford R. Jack, David S. Knopman, William J. Jagust, Ronald C. Petersen, Michael W. Weiner, Paul S. Aisen, Leslie M. Shaw, Prashanthi Vemuri, Heather J. Wiste, Stephen D. Weigand, Timothy G. Lesnick, Vernon S. Pankratz, Michael C. Donohue, and John Q. Trojanowski. Tracking pathophysiological processes in Alzheimer's disease: an updated hypothetical model of dynamic biomarkers. *The Lancet Neurology*, 12(2):207–216, 2013. doi: 10.1016/S1474-4422(12)70291-0.
- [4] Reisa A. Sperling, Paul S. Aisen, Laurel A. Beckett, David A. Bennett, Suzanne Craft, Anne M. Fagan, Takeshi Iwatsubo, Clifford R. Jack, Jeffrey Kaye, Thomas J. Montine, Denise C. Park, Eric M. Reiman, Christopher C. Rowe, Eric Siemers, Yaakov Stern, Kristine Yaffe, Maria C. Carrillo, Bill Thies, Marcelle Morrison-Bogorad, Molly V. Wagster, and Creighton H. Phelps. Toward defining the preclinical stages of Alzheimer's disease: Recommendations from the National Institute on Aging–Alzheimer's Association workgroups on diagnostic guidelines for Alzheimer's disease. *Alzheimer's & Dementia*, 7(3):280–292, 2011. doi: 10.1016/j.jalz.2011.03.003.
- [5] Marilyn S. Albert, Steven T. DeKosky, Dennis Dickson, Bruno Dubois, Howard H. Feldman, Nick C. Fox, Anthony Gamst, David M. Holtzman, William J. Jagust, Ronald C. Petersen, Peter J. Snyder, Maria C. Carrillo, Bill Thies, and Creighton H. Phelps. The diagnosis of mild cognitive impairment due to Alzheimer's disease: Recommendations from the National Institute on Aging–Alzheimer's Association workgroups on diagnostic guidelines for Alzheimer's disease. *Alzheimer's & Dementia*, 7 (3):270–279, 2011. doi: 10.1016/j.jalz.2011.03.008.
- [6] Ronald C. Petersen, Barbara Caracciolo, Carol Brayne, Serge Gauthier, Vesna Jelic, and Laura Fratiglioni. Mild cognitive impairment: a concept in evolution. *Journal of Internal Medicine*, 275(3): 214–228, 2014. doi: 10.1111/joim.12190.
- [7] Alex J. Mitchell and Mojtaba Shiri-Feshki. Rate of progression of mild cognitive impairment to dementia – meta-analysis of 41 robust inception cohort studies. *Acta Psychiatrica Scandinavica*, 119 (4):252–265, 2009. doi: 10.1111/j.1600-0447.2008.01326.x.

- [8] Alex Ward, Sheila Tardiff, Catherine Dye, and H. Michael Arrighi. Rate of conversion from prodromal Alzheimer's disease to Alzheimer's dementia: a systematic review of the literature. *Dementia and Geriatric Cognitive Disorders Extra*, 3(1):320–332, 2013. doi: 10.1159/000354370.
- [9] Giovanni B. Frisoni, Nick C. Fox, Clifford R. Jack, Philip Scheltens, and Paul M. Thompson. The clinical use of structural MRI in Alzheimer disease. *Nature Reviews Neurology*, 6(2):67–77, 2010. doi: 10.1038/nrneurol.2009.215.
- [10] D. P. Devanand, G. Pradhaban, X. Liu, A. Khandji, S. De Santi, S. Segal, H. Rusinek, G. H. Pelton, L. S. Honig, R. Mayeux, Y. Stern, M. H. Tabert, and M. J. de Leon. Hippocampal and entorhinal atrophy in mild cognitive impairment: prediction of Alzheimer disease. *Neurology*, 68(11):828–836, 2007. doi: 10.1212/01.wnl.0000256697.20968.d7.
- [11] Bradford C. Dickerson, Akram Bakkour, David H. Salat, Eric Feczko, Jenni Pacheco, Douglas N. Greve, Francine Grodstein, Christopher I. Wright, Deborah Blacker, H. Diana Rosas, Reisa A. Sperling, Alireza Atri, John H. Growdon, Bradley T. Hyman, John C. Morris, Bruce Fischl, and Randy L. Buckner. The cortical signature of Alzheimer's disease: regionally specific cortical thinning relates to symptom severity in very mild to mild AD dementia and is detectable in asymptomatic amyloid-positive individuals. *Cerebral Cortex*, 19(3):497–510, 2009. doi: 10.1093/cercor/bhn113.
- [12] Clifford R. Jack, Maria M. Shiung, Stephen D. Weigand, Peter C. O'Brien, Jeffrey L. Gunter, Bradley F. Boeve, David S. Knopman, Glenn E. Smith, Robert J. Ivnik, Eric G. Tangalos, and Ronald C. Petersen. Brain atrophy rates predict subsequent clinical conversion in normal elderly and amnesic MCI. *Neurology*, 65(8):1227–1231, 2005. doi: 10.1212/01.wnl.0000180958.22678.91.
- [13] Sean M. Nestor, Ravi Rupasingh, Michael Borrie, Matthew Smith, Vittorio Accomazzi, Jennie L. Wells, Aparna Bhagwat, and Siddhartha Bhattacharyya. Ventricular enlargement as a possible measure of Alzheimer's disease progression validated using the Alzheimer's disease neuroimaging initiative database. *Brain*, 131(Pt 9):2443–2454, 2008. doi: 10.1093/brain/awn146.
- [14] Shannon L. Risacher, Li Shen, John D. West, Sungeun Kim, Brenna C. McDonald, Laurel A. Beckett, Danielle J. Harvey, Clifford R. Jack, Michael W. Weiner, and Andrew J. Saykin. Longitudinal MRI atrophy biomarkers: relationship to conversion in the ADNI cohort. *Neurobiology of Aging*, 31(8):1401–1418, 2010. doi: 10.1016/j.neurobiolaging.2010.04.029.
- [15] Michael W. Weiner, Dallas P. Veitch, Paul S. Aisen, Laurel A. Beckett, Nigel J. Cairns, Robert C. Green, Danielle Harvey, Clifford R. Jack, William Jagust, John C. Morris, Ronald C. Petersen, Andrew J. Saykin, Leslie M. Shaw, Arthur W. Toga, and John Q. Trojanowski. Recent publications from the Alzheimer's Disease Neuroimaging Initiative: Reviewing progress toward improved AD clinical trials. *Alzheimer's & Dementia*, 13(4):e1–e85, 2017. doi: 10.1016/j.jalz.2016.11.007.
- [16] Rik Ossenkoppele, Rik van der Kant, and Oskar Hansson. Tau biomarkers in Alzheimer's disease: towards implementation in clinical practice and trials. *The Lancet Neurology*, 21(8):726–734, 2022. doi: 10.1016/S1474-4422(22)00168-5.
- [17] Ingrid Rye, Alexandra Vik, Marek Kocinski, Arvid S. Lundervold, and Alexander J. Lundervold. Predicting conversion to Alzheimer's disease in individuals with mild cognitive impairment using clinically transferable features. *Scientific Reports*, 12:15566, 2022. doi: 10.1038/s41598-022-18805-5.
- [18] Sara Aghajanian, Farzaneh Mohammadifard, Iman Mohammadi, Saeed Rajai Firouzabadi, Abolfazl Baradaran Bagheri, Ehsan Moases Ghaffary, and Omid Mirmosayyeb. Longitudinal structural MRI-

- based deep learning and radiomics features for predicting Alzheimer’s disease progression. *Alzheimer’s Research & Therapy*, 17(1):182, 2025. doi: 10.1186/s13195-025-01827-2.
- [19] Zhentao Hu, Yong Li, Zheng Wang, Shuo Zhang, and Wei Hou. Conv-Swinformer: Integration of CNN and shift window attention for Alzheimer’s disease classification. *Computers in Biology and Medicine*, 164:107304, 2023. doi: 10.1016/j.combiomed.2023.107304.
- [20] Zhiwei Zhao, Phei Shan Queenie Yeoh, Xianghui Zuo, Joon Huang Chuah, Chee-Onn Chow, Xiang Wu, and Khin Wee Lai. Vision transformer-equipped convolutional neural networks for automated Alzheimer’s disease diagnosis using 3D MRI scans. *Frontiers in Neurology*, 15:1490829, 2024. doi: 10.3389/fneur.2024.1490829.
- [21] Jian Zhou, Yanan Wei, Xin Li, Wei Zhou, Ran Tao, Yiling Hua, and Hongwei Liu. A deep learning model for early diagnosis of Alzheimer’s disease combined with 3D CNN and video Swin transformer. *Scientific Reports*, 15:23311, 2025. doi: 10.1038/s41598-025-05568-y.
- [22] Junhao Wen, Elina Thibeau-Sutre, Mauricio Diaz-Melo, Jorge Samper-González, Alexandre Routier, Simona Bottani, Didier Dormont, Stanley Durrleman, Ninon Burgos, and Olivier Colliot. Convolutional neural networks for classification of Alzheimer’s disease: Overview and reproducible evaluation. *Medical Image Analysis*, 63:101694, 2020. doi: 10.1016/j.media.2020.101694.
- [23] Eric Yee, Da Ma, Karteek Popuri, Lei Wang, and Mirza Faisal Beg. Construction of MRI-based Alzheimer’s disease score based on efficient 3D convolutional neural network: Comprehensive validation on 7,902 images from a multi-center dataset. *Journal of Alzheimer’s Disease*, 79(1):47–58, 2021. doi: 10.3233/JAD-200830.
- [24] Sheng Liu, Arjun V. Masurkar, Henry Rusinek, Jingyun Chen, Ben Zhang, Weicheng Zhu, Carlos Fernandez-Granda, and Navneet Razavian. Generalizable deep learning model for early Alzheimer’s disease detection from structural MRIs. *Scientific Reports*, 12:17106, 2022. doi: 10.1038/s41598-022-20674-x.
- [25] Zhongyi Pei, Zhilei Wan, Yaping Zhang, Minghui Wang, Chengcai Leng, and Yue-Hua Yang. Multi-scale attention-based pseudo-3D convolution neural network for Alzheimer’s disease diagnosis using structural MRI. *Pattern Recognition*, 131:108825, 2022. doi: 10.1016/j.patcog.2022.108825.
- [26] Guilherme Folego, Marina Weiler, Raphael F. Casseb, Rafael Pires, and Anderson Rocha. Alzheimer’s disease detection through whole-brain 3D-CNN MRI. *Frontiers in Bioengineering and Biotechnology*, 8:534592, 2020. doi: 10.3389/fbioe.2020.534592.
- [27] Sina Fathi, Ali Ahmadi, Afsaneh Dehnad, Mostafa Almasi-Dooghaee, and Melika Sadegh. A deep learning-based ensemble method for early diagnosis of Alzheimer’s disease using MRI images. *Neuroinformatics*, 22(1):89–105, 2024. doi: 10.1007/s12021-023-09646-2.
- [28] Giang M. Hoang, Uh-Hyun Kim, and Jae Gwan Kim. Vision transformers for the prediction of mild cognitive impairment to Alzheimer’s disease progression using mid-sagittal sMRI. *Frontiers in Aging Neuroscience*, 15:1102869, 2023. doi: 10.3389/fnagi.2023.1102869.
- [29] Kamilya Kunanbayev, Vivianne Shen, and Dae-Shik Kim. Training ViT with limited data for Alzheimer’s disease classification: An empirical study. In *Medical Image Computing and Computer Assisted Intervention – MICCAI 2024*, volume 15011 of *LNCS*. Springer, 2024. doi: 10.1007/978-3-031-72117-5\_55.

- [30] Vladyslav Gryshchuk, Devesh Singh, Stefan Teipel, and Martin Dyrba. Contrastive self-supervised learning for neurodegenerative disorder classification. *Frontiers in Neuroinformatics*, 19:1527582, 2025. doi: 10.3389/fninf.2025.1527582.
- [31] Francisco J. Martínez-Murcia, Juan M. Gorriz, Javier Ramírez, and Andrés Ortiz. Deep learning prediction of mild cognitive impairment conversion to Alzheimer’s disease at 3 years after diagnosis using longitudinal and whole-brain 3D MRI. *PeerJ Computer Science*, 7:e560, 2021. doi: 10.7717/peerj-cs.560.
- [32] Yucheng Qiu, Mianxin Liu, Liang Huang, Yue Li, Yuanyuan Li, Feng He, Lanxin Lin, Shuicai Chen, Daoqiang Zhang, Qi Guo, and Dinggang Shen. Long-term cognitive decline prediction based on multi-modal data using Multimodal3DSiameseNet: transfer learning from Alzheimer’s disease to Parkinson’s disease. *International Journal of Computer Assisted Radiology and Surgery*, 18(5):809–817, 2023. doi: 10.1007/s11548-022-02829-z.
- [33] Jiahong Chen, Euijoon Kang, Gina Parsons, Arnav Suri, Yucheng Liu, Alisa Chua, Nishant Shah, Anoushka Singh, Zhuo Liu, Harish Ravishankar, Yue Guo, Maged Goubran, Prajakta Bhatt, and Alzheimer’s Disease Neuroimaging Initiative. LongFormer: Longitudinal transformer for Alzheimer’s disease classification with structural MRIs. In *Proceedings of the IEEE/CVF Winter Conference on Applications of Computer Vision (WACV)*, pages 7614–7623, 2024.
- [34] S. Zhang, X. Ding, B. Caffo, J. Chen, X. Zhang, H. Kharrazi, and Z. Wang. Cross-attention fusion of MRI and Jacobian maps for Alzheimer’s disease diagnosis. *arXiv preprint arXiv:2503.00586*, 2025. URL <https://arxiv.org/abs/2503.00586>.
- [35] Jiahong Ouyang, Qingyu Zhao, Courtney K. Bass, Ehsan Adeli, Greg Zaharchuk, Michael D. Greicius, Kathleen L. Poston, and Kilian M. Pohl. Stochastic Siamese MAE pretraining for longitudinal medical images. *Medical Image Analysis*, 99:103370, 2025. doi: 10.1016/j.media.2024.103370.
- [36] Xiangrui Li, Paul S. Morgan, John Ashburner, Jolinda Smith, and Christopher Rorden. The first step for neuroimaging data analysis: DICOM to NIfTI conversion. *Journal of Neuroscience Methods*, 264: 47–56, 2016. doi: 10.1016/j.jneumeth.2016.03.001.
- [37] Nicholas J. Tustison, Philip A. Cook, Andrew J. Holbrook, Hans J. Johnson, John Muschelli, Gabriel A. Devenyi, Jeffrey T. Duda, Sandhitsu R. Das, Nicholas C. Cullen, Daniel L. Gillen, Michael A. Yassa, James R. Stone, James C. Gee, and Brian B. Avants. The ANTsX ecosystem for quantitative biological and medical imaging. *Scientific Reports*, 11(1):9068, 2021. doi: 10.1038/s41598-021-87564-6.
- [38] Brian B. Avants, Nicholas J. Tustison, Gang Song, Philip A. Cook, Arno Klein, and James C. Gee. A reproducible evaluation of ANTs similarity metric performance in brain image registration. *NeuroImage*, 54(3):2033–2044, 2011. doi: 10.1016/j.neuroimage.2010.09.025.
- [39] Jingyuan Wang, Fei Gao, Jiangchang Dong, Qian Zhang, Haipeng Wang, and Guangzhi Ma. AFS-Net: Attention-guided 3d CNN with lesion feature selection for early Alzheimer’s disease prediction. *Computers in Biology and Medicine*, 184:109395, 2025. doi: 10.1016/j.compbiomed.2024.109395.
- [40] Esther E. Bron, Marion Smits, Wiro J. Niessen, and Stefan Klein. Cross-cohort generalizability of deep and conventional machine learning for MRI-based diagnosis and prediction of Alzheimer’s disease. *NeuroImage: Clinical*, 31:102712, 2021. doi: 10.1016/j.nicl.2021.102712.
- [41] Weiming Lin, Tong Tong, Qinquan Gao, Di Guo, Xiaofeng Du, Yonggui Yang, Gang Guo, Min Xiao, Min Du, and Xiaobo Qu. Convolutional neural networks-based MRI image analysis for the Alzheimer’s

- disease prediction from mild cognitive impairment. *Frontiers in Neuroscience*, 12:777, 2018. doi: 10.3389/fnins.2018.00777.
- [42] Simeon Spasov, Luca Passamonti, Andrea Duggento, Pietro Liò, and Nicola Toschi. A parameter-efficient deep learning approach to predict conversion from mild cognitive impairment to Alzheimer’s disease. *NeuroImage*, 189:276–287, 2019. doi: 10.1016/j.neuroimage.2019.01.031.
- [43] Manhua Liu, Fan Li, Hao Yan, Kefeng Wang, Yixin Ma, Li Shen, and Mingxia Xu. Predicting Alzheimer’s disease conversion from mild cognitive impairment using an extreme learning machine-based grading method with multimodal data. *Frontiers in Aging Neuroscience*, 12:77, 2020. doi: 10.3389/fnagi.2020.00077.
- [44] Garam Lee, Kwangsik Nho, Byungkon Kang, Kyung-Ah Sohn, and Dokyoon Kim. Predicting Alzheimer’s disease progression using multi-modal deep learning approach. *Scientific Reports*, 9(1):1952, 2019. doi: 10.1038/s41598-018-37769-z.
- [45] Yanru Chen, Xiaoyu Qian, Yuanyuan Zhang, Wenli Su, Yumeng Huang, Xinyu Wang, Xiaoping Chen, Enyan Zhao, Lu Han, and Yuxia Ma. Prediction models for conversion from mild cognitive impairment to Alzheimer’s disease: a systematic review and meta-analysis. *Frontiers in Aging Neuroscience*, 14: 840386, 2022. doi: 10.3389/fnagi.2022.840386.
- [46] Yifan Wang, Ruitian Gao, Ting Wei, Luke Johnston, Xin Yuan, Yue Zhang, and Zhangsheng Yu. Predicting long-term progression of Alzheimer’s disease using a multimodal deep learning model incorporating interaction effects. *Journal of Translational Medicine*, 22(1):265, 2024. doi: 10.1186/s12967-024-05025-w.
- [47] Sara Fin, Alireza Moayedikia, and Uffe Kock Wiil. Dual-model deep learning for Alzheimer’s prognostication. *Computers in Biology and Medicine*, 208:111672, 2026. doi: 10.1016/j.compbiomed.2026.111672.
- [48] Alireza Moayedikia, Sara Fin, and Uffe Kock Wiil. Multi-objective optimization formulation for Alzheimer’s disease trial patient selection. *Journal of Biomedical Informatics*, 172:104955, 2025. doi: 10.1016/j.jbi.2025.104955.
- [49] Heiko Braak and Eva Braak. Neuropathological stageing of Alzheimer-related changes. *Acta Neuropathologica*, 82(4):239–259, 1991. doi: 10.1007/BF00308809.
- [50] Susanne Dandl, Christoph Molnar, Martin Binder, and Bernd Bischl. Multi-objective counterfactual explanations. In *Parallel Problem Solving from Nature – PPSN XVI*, pages 448–469. Springer, 2020. doi: 10.1007/978-3-030-58112-1\_31.
- [51] Ali Ebrahimi, Uffe Kock Wiil, Tomas Olsson, Pietro Liò, Ingrid Kockum, Ali Manouchehrinia, and Narsis A. Kiani. A susceptibility network analysis of disease trajectories leading to multiple sclerosis: A nationwide cohort study. *Multiple Sclerosis Journal*, pages 1–12, 2026. doi: 10.1177/13524585261421480.